

Dominantly Aseismic Nucleation of Laboratory Earthquakes: A Quantitative Investigation

S. Marty¹, H. S. Bhat¹, J. Aubry¹, E. Fukuyama^{2,3}, R. Madariaga¹, A. Schubnel¹

¹Laboratoire de Géologie, Ecole Normale Supérieure, CNRS-UMR8538, PSL Research University, Paris

²National Research Institute for Earth Science and Disaster Resilience, Tsukuba, Ibaraki 305-0006, Japan

³Department of Civil and Earth Resources Engineering, Kyoto University, Kyoto 615-8530, Japan

Key Points:

- AE precursors to stick-slip instabilities are recorded using calibrated acoustic sensors
- The seismic component of the nucleation phase is positively correlated with fault surface roughness
- Nucleation is an almost fully aseismic process

arXiv:submit/3737070 [physics.geo-ph] 10 May 2021

Corresponding author: S. Marty, sam92son@gmail.com

Abstract

Decades of seismological observations have highlighted the variability of foreshock occurrence prior to natural earthquakes, making thus difficult to track how earthquakes start. Here, we report on three stick-slip experiments performed on cylindrical samples of Indian metagabbro under upper crustal stress conditions (30-60 *MPa*). Acoustic emission activity (AE) was continuously recorded by 8 calibrated acoustic sensors during the experiments, and the seismological parameters (moment magnitude, corner frequency and stress-drop) of the detected AEs were estimated. The scaling law between moment magnitude and corner frequency that characterizes natural earthquakes also applies to the detected AEs ($-8.8 \leq Mw \leq -7$). AE data were analysed in terms of AE timing and locations, released moment via AEs and AE frequency-magnitude distribution. These aforementioned features were interpreted with regard to fault surfaces roughness and microstructure, along fault slip and slip velocity. Precursory AE activity is systemically detected during the pre-failure period, increases towards failure and is found to be driven by along fault slip velocity. Consistently for all three experiments, the stacked AE sequences follow an inverse power law of the time to failure. AEs moment magnitudes increase as shear-stress rises prior to stick-slip instabilities, as manifested by b-value decrease. At the lowest stress condition, the fault surface was characterized by an higher long wavelength roughness due to gouge particles accumulation, which constitutes an higher degree of fault strength heterogeneity. Increasing fault strength heterogeneity results in larger generated AEs, smaller b-value and higher coupling. Decreasing fault strength heterogeneity promotes, on average, AEs migration towards zones where stick-slip events initiate. Overall, the seismic component of the pre-failure phase differs by several orders of magnitude from the aseismic component. Our observations suggest that, in this particular experimental setting, precursory AE activity is predominantly triggered by the larger nucleation phase of the upcoming stick-slip event which is an almost fully aseismic process.

Abstract

Decades of seismological observations have highlighted the variability of foreshock occurrence prior to natural earthquakes, making thus difficult to track how earthquakes start. Here, we report on three stick-slip experiments performed on cylindrical samples of Indian metagabbro under upper crustal stress conditions (30-60 MPa). Acoustic emission activity (AE) was continuously recorded by 8 calibrated acoustic sensors during the experiments, and the seismological parameters (moment magnitude, corner frequency and stress-drop) of the detected AEs were estimated. The scaling law between moment magnitude and corner frequency that characterizes natural earthquakes also applies to the detected AEs ($-8.8 \leq Mw \leq -7$). AE data were analysed in terms of AE timing and locations, released moment via AEs and AE frequency-magnitude distribution. These aforementioned features were interpreted with regard to fault surfaces roughness and microstructure, along fault slip and slip velocity. Precursory AE activity is systemically detected during the pre-failure period, increases towards failure and is found to be driven by along fault slip velocity. Consistently for all three experiments, the stacked AE sequences follow an inverse power law of the time to failure. AEs moment magnitudes increase as shear-stress rises prior to stick-slip instabilities, as manifested by b-value decrease. At the lowest stress condition, the fault surface was characterized by an higher long wavelength roughness due to gouge particles accumulation, which constitutes an higher degree of fault strength heterogeneity. Increasing fault strength heterogeneity results in larger generated AEs, smaller b-value and higher coupling. Decreasing fault strength heterogeneity promotes, on average, AEs migration towards zones where stick-slip events initiate. Overall, the seismic component of the pre-failure phase differs by several orders of magnitude from the aseismic component. Our observations suggest that, in this particular experimental setting, precursory AE activity is predominantly triggered by the larger nucleation phase of the upcoming stick-slip event which is an almost fully aseismic process.

1 Introduction

The term “foreshocks” refers to small earthquakes that would occur nearby in time and space of a larger earthquake to come. (Papazachos, 1973) made the observation that when a sufficient number of foreshock sequences were synchronized to the time of their respective main shock and then stacked, the seismicity rate increases as an inverse power law of time when approaching the nucleation. This law, called “the inverse Omori law”, had then provided a potential path to earthquake prediction. Since that time, a lot of effort have been made to understand the driving forces of foreshock occurrence.

Crustal earthquakes are dynamic instabilities which result from the weakening of frictional properties of a seismogenic fault that has started to slip. The relation between on-fault friction and slip provides the theoretical frame to understand how earthquakes nucleate. Based on either slip weakening or rate-and-state friction laws, theoretical (Ida, 1972; Campillo & Ionescu, 1997; Uenishi & Rice, 2003) and numerical models (Rubin & Ampuero, 2005; Ampuero & Rubin, 2008) have demonstrated that before propagating dynamically, slip initially develops on a localized, slowly growing zone, which is defined as the nucleation zone. A large number of stick-slip experiments have supported this conceptual view of earthquake nucleation, whether it is for experiments conducted at low normal stress conditions on synthetic materials (Latour et al., 2013; Nielsen et al., 2010) or on crustal rocks (Okubo & Dieterich, 1984; Ohnaka & Kuwahara, 1990; Ohnaka, 2003; McLaskey & Kilgore, 2013; Fukuyama et al., 2018).

Although rupture nucleation is a process thought to be aseismic, laboratory friction experiments (Thompson et al., 2009; McLaskey & Lockner, 2014; Kwiatek et al., 2014; Passelègue et al., 2017) have found the acoustic emission (AE) rate to be correlated to aseismic slip propagation and have reinforced the possibility of earthquake

forecasting. Experimental works have also investigated changes in the frequency-magnitude distribution (i.e. the b-value of the Gutenberg-Richter slope) of AEs during stick-slip cycles. When the shear stress increases and the rupture is developing, a significant drop of the b-value has been reported, i.e. the ratio between large and small AEs increases (W. Goebel et al., 2013; Rivière et al., 2018; Lei et al., 2018). This was thought to be driven by accelerating slip before dynamic rupture propagation. Consequently, this indicates that b-value changes could be used as a tool for seismic hazard assessment. However, under the assumption that foreshocks only reflect nucleation processes, it is necessary to constrain the length and time scales over which earthquakes nucleate.

In the frame of rate-and-state friction laws, models that use laboratory derived friction parameters predict that earthquakes nucleate on short time and space scales, of the order of milliseconds and meters respectively (Lapusta & Rice, 2003; Kaneko & Lapusta, 2008; Fang et al., 2010). This is a consequence of the characteristic slip distance D_c (i.e. the length required for the friction to reach its residual value inferred from rock friction experiments being of the order of 1-100 μm). In the former case, detecting earthquakes nucleation from geodetic or seismological measurements would likely be unreachable. On the other hand, seismological observations have suggested that D_c should be scale dependent (Ide & Takeo, 1997; Olsen et al., 1997), of the order of the centimeter at the scale of crustal earthquakes. The scaling of D_c has been attributed to length scales inherent to the size of earthquakes such as long wavelength roughness of fault zones (Ohnaka, 2003) or gouge thickness (Marone, 1998). If we consider that the critical slip distance involved during coseismic slip is the same that governs earthquake nucleation (Cocco et al., 2009), this would imply nucleation processes to happen at much larger length and time scales.

At the scale of crustal earthquakes, numerous seismological observations have reported on increasing foreshock activity preceding the occurrence of large earthquakes (L. Jones & Molnar, 1976; Abercrombie & Mori, 1996; Bouchon et al., 2011; Kato & Nakagawa, 2014). Foreshock activity preceding large subduction earthquakes has been found to correlate with the occurrence of slow slip transients in the region close to the hypocenter (Kato et al., 2012; Ruiz et al., 2014). When examining the occurrence of foreshock sequences with respect to the geodynamic context, it has been demonstrated that faults subject to high-slip rates produce more foreshock sequences (McGuire et al., 2005; Bouchon et al., 2013). Moreover, compared with the ordinary seismicity, foreshocks present singular characteristics such as migration and acceleration prior to the mainshock (Marsan et al., 2014; Kato et al., 2016). Therefore, it has been argued that foreshocks are a by-product of the larger nucleation of the upcoming mainshock. However, because of the sparsity of the observations, the physical processes that govern the occurrence of foreshocks are still controversial. For instance, statistical ETAS models (Ogata, 1988; Helmstetter & Sornette, 2003b) are able to reproduce most of the features attributed to foreshock sequences which was used as an argument to suggest that foreshocks reflect stochastic rather than physical processes. One of the underlying questions is whether or not earthquakes are preceded by a slow, emerging nucleation phase before propagating dynamically or start as small instabilities that may eventually grow bigger. These two opposite views are termed the "preslip" and the "cascade" models respectively (Ellsworth & Beroza, 1995; Beroza & Ellsworth, 1996). In the latter scenario, the use of foreshocks as a predictive tool for the occurrence of a larger earthquake would be compromised.

Here we report on precursory AE sequences during stick-slip experiments conducted on metagabbro saw-cut samples and under crustal stress conditions (30, 45 and 60 MPa). The purpose of this study is to use generated precursory AEs as a proxy to investigate the dominant mechanisms that control foreshock dynamics. Using calibrated acoustic sensors, AE seismological parameters (absolute moment magnitude, corner frequency, source size and stress drop) are estimated. AE features such as magnitude-frequency distribution, spatial distribution and temporal evolution towards failure are

examined and interpreted with regard to along fault premonitory deformation, fault surface roughness and post-experiment fault structure. At last, we rely on absolute AE moment magnitudes to estimate the ratio between the seismic and the aseismic components of the pre-failure phase.

2 Experimental set-up and methodology.

Here, we describe the experimental set-up that we used to produce stick-slip events (SSEs) and the methods used to analyse and process the data.

2.1 Tri-axial press and external measurements.

Stick-slip experiments were conducted on saw-cut samples of Indian metagabbro under tri-axial conditions. The tri-axial apparatus used is described in details in the supplementary materials (text and figure S1). Saw cut samples were axially loaded at constant strain rate of about $4 \cdot 10^{-6}$ (about 0.02 MPa/s). Pressure sensors positioned outside of the cell allowed us to measure the axial stress and the confining pressure from which we calculated the average macroscopic shear stress, the macroscopic normal stress and the friction coefficient acting onto the fault plane (text S1). Displacement was measured by a LVDT at the top of the axial piston and thus includes the elastic shortening of the whole system (i.e. apparatus + sample). Along fault displacement was calculated by correcting the overall displacement from the elastic shortening of the axial piston and the sample (text S1). Stresses and displacement were measured at 10 Hz sampling rate with respectively $\pm 0.001 \text{ MPa}$ resolution and $\pm 0.1 \mu\text{m}$ of resolution.

2.2 Acoustic recording system.

The acoustic wave-field was continuously recorded at 10 MHz sampling rate by 8 acoustic sensors (figure S2). AEs were detected within the continuous acoustic waveforms (text S2, supp. mat.). Note that we opted to position all the acoustic sensors on the same half of the sample so their relative positions do not change with cumulative displacement. Acoustic signals were amplified at 45 dB, i.e. by a factor of about 177. This allowed us for recording the microseismicity close to the noise level. Local strain measurements were also continuously measured at 10 MHz sampling rate by 8 single component strain gauges located on both sides of the fault. It should be noted that here we only focus on acoustic measurements, strain gauges data will be further analyzed in a future study.

2.3 AE source localization.

AEs locations were inverted according to first P-wave arrivals (Text S3, supp. mat.). We made the assumption that all AEs came from the fault (i.e. 2-D grid search) which seems a reasonable assumption given that (i) by localizing the AEs with a 3-D grid search, we found that AE locations align with the fault plane and (ii) we often observed positive and negative first P-wave polarities (except for AEs located at one edge of the fault plane) which indicates double-couple seismic sources. The smallest AEs could not be located due to their first P-wave arrivals really close to the noise level and not easily distinguishable. The location procedure was thus restricted to AEs with sufficiently high-amplitude and impulsive first P-wave arrivals.

2.4 Acoustic sensors calibration.

Waveforms recorded by an uncalibrated acoustic sensor have a unit of voltage and part of the information reflects sensor's sensitivity. Therefore, estimating AE

seismological parameters requires acoustic sensor calibration. Acoustic sensor calibration aims to obtain acoustic sensor's sensitivity function that can be used (i) to convert voltage measurement into absolute measurements (displacement, velocity or acceleration) and (ii) to correct for variations of sensor's sensitivity with frequency. In what follows we briefly describe the methodology to calibrate the acoustic sensor's and the principal results obtained. A detailed description of the methodology and the experimental set-up is given in the supplementary material (figure S1, text s1).

The sensitivity function of the acoustic sensors was obtained by laser interferometry. Outside of the cell, we affixed a broadband transducer to the center of the simulated fault surface (figure s1). Then a step voltage was applied to the broadband transducer and vibration of the opposite surface of the sample was measurement by one of the acoustic sensor used in the experiments. Then the acoustic sensor was removed and surface vibration (i.e. at the same location) was recorded by a Laser Doppler Vibrometer which was set to measure particle velocity with a flat instrumental response from 0 to 2.5 *MHz*. The sensitivity function of the acoustic sensor $I_a(f)$ was obtained in frequency domain by deconvolution of the waveform recorded by the acoustic sensor $S_a(f)$ out of the waveform recorded by the LDV $S_v(f)$:

$$I_a(f) = \frac{S_a(f)}{S_v(f)} \quad (1)$$

Therefore $I_a(f)$ acts as a transfer function and can be used to convert the waveforms $S_a(f)$ recorded by the acoustic sensors into particle velocity measurements $S_c(f)$, such as (in frequency domain):

$$S_c(f) = \frac{S_a(f)}{I_a(f)} \quad (2)$$

Since we expected AEs to have variable moment magnitudes and source duration we examined the variability of the acoustic sensors sensitivity function with the size of the source, its amplitude and its duration. Two types of broadband acoustic transducers (namely, V109-rm and M110-sm), designed by the Olympus company, were used as a source. Both transducers had a similar central frequency of 5 *MHz* but differed by their size: the transducer V109-RM has a nominal element size of 13 *mm* while M110-RM has a nominal element size of 6 *mm* (see supp. mat.). Figure 2 summarizes the calibration results that we obtained. The calibration curves were obtained for two input voltages, 40 V and 200 V and for three source durations, 2 μs , 1 μs and 0.5 μs (i.e. 0.5*MHz*, 1 *MHz* and 2 *MHz*). For the same type of source, we observed no significant differences with respect to the amplitude and the duration of the input voltage. All calibration curves almost collapse (Figures 2a, b). Figure 2c, displays the sensitivity function averaged over all input voltages and source durations for both transducers. In both case, it is clear that the sensitivity of the acoustic sensors shows non linearity, with a wide resonance band between about 1.2 and 2.2 *MHz*. This might be related to the specific properties of the PZT ceramics. Above 1 *MHz*, wavelengths are of the order of few millimeters which lies in the range of the length scales that characterize the acoustic sensor casing. This could also induce strong sensitivity variations at high-frequency. Although the sensitivity functions are quite similar up to 1 *MHz*, some differences emerge when increasing frequency. In the case of the larger source, V109-rm, the resonance band is narrower and the sensitivity function decreases to a lower value after the maximum peak. A larger source size is equivalent to the multiple point source scenario that would generate waves at the same time. This might reduce the curvature of the wavefronts and induce negative interferences with increasing frequency. Although AE sources can be of different sizes, we posit that the synchronized multiple source point scenario is unlikely. For this reason we chose to use the sensitivity function obtained in the case of the smaller source, M110-sm.

2.5 Inversion of AE paramameters

Seismic parameters estimation relies on the analysis of displacement spectra to estimate the absolute magnitude of the source, its size and stress-drop. Seismological parameters were obtained based on S-wave displacement spectra since we expect that most of the energy comes from S-waves.

Acoustic waveforms were analysed within a $27.5 \mu s$ time window occurring $2.5 \mu s$ before the theoretical S-wave arrival times. The energy contained between the beginning of the selected time-window and the S-wave arrival was damped with a ramp function to reduce energy related to P-waves. The selected time window was then rescaled to a $50 \mu s$ time window centered to the theoretical S-wave arrival and multiplied by a von Hann window (Figure 4 b.). This allows us to lower energy contributions coming from reflections and surface waves. We obtained S-wave displacement spectra $\Omega_s(f)$ by first averaging over all acoustic sensors the spectra corrected by deconvolution with the estimated sensitivity function $I_a(f)$. The final displacement spectra were then obtained by integration in frequency domain. This takes the form:

$$\Omega_s(f) = \frac{\sum_{k=1}^K S_k^{as}(f)}{K \cdot I_a(f)} \cdot \frac{1}{2\pi f} \quad (3)$$

where K corresponds to the total number of acoustic sensors and $S_k^{as}(f)$ to the spectrum of the k 'th acoustic waveform. The next step was to fit the S-wave displacement spectra with a Brune model corrected for attenuation. The S-wave displacement spectra $\Omega_s(f)$ were modelled as:

$$\Omega_s(f) = \Omega_0 \exp(-\pi f t / Q) \cdot \frac{1}{1 + (f/f_c)^2} \quad (4)$$

where Ω_0 is the long period spectral plateau, t is the averaged S-wave travel time, Q the attenuation factor and f_c the corner frequency. Ω_0 , f_c and Q were estimated by performing a grid search over the three parameters. Here, Q is an important parameter because it controls the high-frequency decay together with the corner frequency f_c . Therefore, to avoid significant trade-offs between Q and f_c we limited Q search from 30 to 50 based on values found in the literature (Goldberg et al., 1992; Liu & Ahrens, 1997; Yoshimitsu et al., 2014). Search ranges were from 10^{-18} to $10^{-15} m.s$ for Ω_0 and 100 kHz to 2.5 MHz for f_c . The seismic moment was computed from Ω_0 according to:

$$M_0 = \frac{4 \cdot \pi \cdot \rho \cdot C_s \cdot R \cdot \Omega_0}{\Lambda_{\theta, \phi}} \quad (5)$$

where ρ is the density, C_s the shear wave velocity, R the averaged distance and $\Lambda_{\theta, \phi}$ the averaged S wave radiation pattern (0.63, (Aki & Richards, 2002)). From M_0 we obtained the absolute moment magnitude as:

$$M_w = (\log_{10}(M_0) - 9.1) / 1.5 \quad (6)$$

Assuming the circular crack model of Madariaga (Madariaga, 1976), the radius of the seismic source is calculated from f_c such as:

$$r = \frac{0.21 \cdot C_s}{f_c} \quad (7)$$

Finally, the stress drop $\Delta\sigma$ was computed as a function of the seismic moment and the radius of the source as (Eshelby, 1957):

$$\Delta\sigma = \frac{7M_0}{16r^3} \quad (8)$$

Figure 4a displays an example of fitted displacement spectra for two events of magnitudes $Mw - 7.7$ and $Mw - 8.6$ and the associated waveforms. Corner frequencies were found to be 0.88 MHz and 1.5 MHz , respectively, which yields source radius of the order of 0.8 mm and 0.45 mm respectively. Estimated stress drops are approximately 0.75 MPa for the $Mw - 8.6$ event and 3.35 MPa for the $Mw - 7.7$ which is in the range of those observed for natural earthquakes. The absence of the resonance band in the displacement spectra (Figure 4a) confirms in part that the sensitivity function was well estimated.

3 Results

For the sake of clarity we explain here the next term that will come up frequently in what follows: "Normalized time to failure". The normalized to failure refers to the time prior to failure divided by the total duration of loading.

3.1 Mechanical data

Three experiments were performed at varying confining pressures, P_c : 30, 45 and 60 MPa . Figures 5a, b and c display the evolution of shear-stress, along fault cumulative displacement and AE rate at $P_c = 30, 45$ and 60 MPa respectively.

At $P_c = 30\text{ MPa}$ (Figure 5a) we have reproduced a sequence of 55 SSEs. The first one occurred when the macroscopic shear-stress was about 22 MPa , this equates to a static friction coefficient of 0.5. The associated coseismic displacement was $31\text{ }\mu\text{m}$. From the beginning to the end of the experiment, the maximum shear-stress (i.e. the shear stress at the time of the rupture) has increased from 22 to 36 MPa which corresponds to an increase of the static friction coefficient from 0.5 to 0.7. Although the static friction coefficient continuously increased with successive SSEs, it started to stabilize after approximately 5 mm of cumulative displacement. At the beginning of the experiment we recorded only a few AEs in the last second prior to dynamic rupture propagation. This can be observed by the relatively low acoustic activity that only arises close to stick-slip instabilities. Then, up to the end of the experiment, the acoustic activity intensified. One interesting feature is that the acoustic activity started to occur earlier but at a lower rate when the static friction coefficient started to stabilize.

At $P_c = 45\text{ MPa}$ (Figure 5b) we have reproduced a sequence of 29 SSEs. The mechanical behavior of the rock specimen has shown some similarities with the one at $P_c = 30\text{ MPa}$. The first SSE occurred at relatively low stress conditions, when the shear stress was about 32 MPa which corresponds to a static friction coefficient of 0.5. The corresponding coseismic displacement was $58\text{ }\mu\text{m}$. Then the maximum shear stress has increased from 32 to 51 MPa which equates to an increase of the static friction coefficient from 0.5 to 0.68. Quite remarkably, similarly to the experiment at $P_c = 30\text{ MPa}$ the static coefficient of friction has approximately stabilized after 5 mm of cumulative displacement. Regarding the acoustic activity, the AE rate has rapidly increased with the successive stick-slip cycles. However a noticeable difference with the experiment conducted at $P_c = 30\text{ MPa}$ is that the AEs remained concentrated in the last 2-3 seconds prior to stick-slip instabilities.

At $P_c = 60\text{ MPa}$ (Figure 5c) we have reproduced a sequence of 13 SSEs. The mechanical behavior of the sample has shown significant differences with the experiments at $P_c = 30\text{ MPa}$ and $P_c = 45\text{ MPa}$. The first SSE happened when the shear stress reached 64 MPa and the static friction coefficient 0.65. The corresponding coseismic slip was $184\text{ }\mu\text{m}$. After the first SSE, the static friction coefficient oscillated between 0.65 and 0.72 and was almost constant for the last 5 SSEs. The AE rate has largely fluctuated from the beginning to the end of the experiment. Prior to particular SSEs (SSEs 9 and 13 for instance) we recorded intense bursts of AEs while for other

SSEs the AEs rate preceding failure remained low (SSEs 11, 12 and 13). AEs mostly happened during the last 1-2 seconds prior to failure.

3.2 AEs distribution

Figure 6 displays the number of precursory AEs recorded (left) and the total AE moment release (right) per SSE. The total AE moment that we show here is likely to be underestimated for particular SSEs because acoustic sensor recordings started to saturate for moment magnitudes M_w higher than -7, although for such a magnitude we usually observed that only few acoustic sensors were saturating. Star symbols mark the SSEs prior to which we recorded at least one AE with moment magnitude M_w higher than -7 (in total, 23 at $P_c = 30$ MPa, 5 at $P_c = 45$ MPa and 2 at $P_c = 60$ MPa).

The total number of AEs recorded during the experiments is 905, 380 and 185 for respectively $P_c = 30$, 45 and 60 MPa. This equates to an average number of AEs per SSE of about 17, 13 and 14 respectively. As we could have expected according to the AE rate presented in figure 5, the number of AEs per stick-slip cycle fluctuates somewhat but tends to increase with the successive SSEs although it is less significant at $P_c = 60$ MPa. The maximum number of precursory AEs within one sequence (i.e. for one SSE) that we recorded is 48, 31 and 46 at $P_c = 30, 45$ and 60 MPa respectively.

The total AE moment per SSE depicts a different picture. A common feature to all the experiments is that the seismic energy released can largely vary from one precursory AEs sequence to another. At the early stage of the experiments conducted at $P_c = 30$ and 45 MPa we only recorded small AEs, which corresponds to the periods during which the static friction coefficient on the fault increased relatively fast. Then, we recorded oscillations between low and high energy AE sequences. During the experiment conducted at $P_c = 60$ MPa the seismic energy released onto the fault prior to stick-slip instabilities was slightly more stable (for instance from SSE 8 to SSE 12) but has shown significant variations as well.

A notable feature is that we recorded more large AEs during the experiment conducted at $P_c = 30$ MPa compared to $P_c = 45$ and 60 MPa (note that for visualization, the axis of the total AE moment release is different at $P_c = 30$ MPa). The maximum precursory AE moment release that we estimated for a single sequence was 0.8 N.m at $P_c = 30$ MPa and 0.18 N.m at both $P_c = 45$ and 60 MPa. We recall that these values are lower bounds due to the saturation of acoustic sensors.

Figure 7 shows the frequency-magnitude distributions of the recorded AEs (blue, red and black circles correspond to $P_c = 30, 45$ and 60 MPa respectively). The colored circles indicate the cumulative Gutenberg-Richter (G-R) distribution of the estimated AEs magnitudes and the bar plots display their distribution into 0.1 magnitude interval bins. We estimated that the magnitude of completeness M_c was close to $M_w = -8.7$. M_c might vary a little depending on the confining pressure (for instance between $P_c = 30$ and $P_c = 45$ MPa) but it is not significant given that the typical error in magnitude estimation was 0.1. The black arrows indicate the upper limit magnitude ($M_w = -7$) beyond which acoustic sensors started to saturate. The estimated moment magnitudes M_w went beyond $M_w = -7$ for 71 AEs during the experiment conducted at $P_c = 30$ MPa, for 6 AEs at $P_c = 45$ MPa and for 5 AEs at $P_c = 60$ MPa. As mentioned earlier, we found from visual inspection that not all acoustic sensors were saturating for AEs with $M_w \approx -7$. Moreover, acoustic waveforms were saturating only for a short period (10 μ s typically). Therefore we believe that close to this upper limit magnitude, our estimations are not significantly biased. However, beyond $M_w = -6.8$ almost all acoustic sensors were saturating over a large portion of the signal, which in the former case unambiguously indicates a significantly larger moment magnitude. Such a case only happened during the experiment conducted at $P_c = 30$ MPa, for 21 AEs.

Using $M_c = -8.7$ we estimated the G-R b-value based on the Aki-Utsu maximum likelihood method (Aki, 1965; Utsu 1965). The best fits we obtained are given by the black dashed lines and are $b = 0.57 \pm 0.02$, $b = 0.65 \pm 0.03$ and $b = 0.66 \pm 0.04$ at $P_c = 30$, 45 and 60 *MPa* respectively. The experiments conducted at $P_c = 45$ *MPa* and $P_c = 60$ *MPa* show a similar AEs G-R distribution with a net decrease of the number of AEs beyond $M_w = -7.6$. This is in sharp contrast with the experiment conducted $P_c = 30$ *MPa* which is characterized by a significant larger number of AEs beyond $M_w = -7.6$. Quite remarkably, at $P_c = 30$ *MPa* the AEs G-R distribution tends to follow a double distribution.

3.3 AE and stick-slip nucleation locations

Figure 8 displays on the left the photographs of the simulated faults after the experiments. AE (circles) and stick-slip nucleation (stars) locations onto the fault planes are shown at the center and on the right respectively. The colorscale refers to the SSE index. The size of the circles was set according to the estimated moment magnitudes. Assuming a circular source shape, the typical source sizes for a $M_w = -7$ AE and for a $M_w = -8$ AE are about 3 *mm* and 1 *mm* respectively. Only the AEs for which the residual times were less than 0.3 μs (which equates to 2-3 *mm* of location accuracy) are shown. Therefore large AEs are over represented on the figure.

The fault surface at $P_c = 30$ *MPa* is the one that presents the largest amount of gouge particles. Gouge particles have aggregated into patches of various sizes, as illustrated by the white patterns elongated in the direction of sliding. The gouge particle clusters tend to concentrate in the middle of the fault and have a characteristic size in the order of few millimeters. It should be noted that we looked at the other surface condition and both surfaces were symmetrical. Therefore, zones without gouge particles are not due to gouge removal when the two pieces of the rock specimen were separated after the experiments. AEs correlate well with areas where gouge particles are concentrated. However, there are zones covered with gouge particles where no AEs were detected (for instance on the area on the top part of the fault). Quite remarkably, we can observe that SSEs nucleated in the same area at the early stage of the experiment and then migrated to another region. An easily observable feature is that the SSEs at the last stage of the experiment (warm colors) tend to nucleate at the edges of the areas where most of the precursory AE moment was released.

The simulated fault at $P_c = 45$ *MPa* presents less gouge particles compared to the experiment conducted at $P_c = 30$ *MPa*. We still observe patches where gouge particles concentrate but these are more heterogeneously distributed on the fault. Similarly to the experiment conducted at $P_c = 30$ *MPa* there are areas covered by gouge particles where few or no AEs were detected (for instance, on the lower edge of the fault on the left). Because there are less AEs here, it is easier to observe that their locations mirror fairly well the geometry of the areas covered by gouge particles. In the same way than the experiment conducted at $P_c = 30$ *MPa*, SSEs nucleation migrated over time (from the left edge of the fault plane to the right edge). We can observe as well that SSEs do not necessarily nucleate where most of the AE activity is concentrated.

At $P_c = 60$ *MPa*, gouge particles are homogeneously distributed over the fault surface. Unlike the other two experiments, we no longer observe patches of gouge particles. AEs tend to locate in a reduced region of the fault surface with respect to the other two experiments. In that case, we can observe migration of the AE activity (from the left to the right) with the successive ruptures, which seems roughly correlated with SSEs nucleation locations.

3.4 Microstructural analysis

Figure 9 displays the post-mortem fault surfaces observed by scanning electron microscopy (SEM). The large scale view of the fault surfaces at $Pc = 30$ MPa and $Pc = 45$ MPa (Figures 9b and d respectively) reveals highly damaged zones with a large quantity of generated gouge particles that cluster into patches. Gouge particles present a typical size ranging from less than $1 \mu m$ to few μm (Figure 9a) and cover topographic highs with size of the order of few tens of μm (Figure 9b) that we might interpret as small scales asperities. The enlarged view of the fault surface at $Pc = 60$ MPa (Figure 9f) also reveals fine gouge particles production but the latter are not aggregated but rather homogeneously distributed on top of stretched and elongated surfaces in the direction of sliding. Zooming on the fault surface at $Pc = 60$ MPa (Figure 9e) allows us to observe stringy microstructures that contain gas bubbles. This suggests partial melting of the fault surface during slip. The micro-crack that crosses the residual melt results likely to the rapid cooling following melting. We can observe that a fraction of the small gouge particles is trapped into the melt. At $Pc = 45$ MPa the fault surface displays elongated patterns in the direction of sliding as well (Figure 9d) which presupposes that fault surface temperature has nearly reached the melting point. At smaller scale (Figure 9c), the fault surface has compacted and flattened microstructures that align with the direction of slip which we interpret as markers of plastic deformation processes.

3.5 Fault surface roughness analysis

Fault surfaces roughness were accurately measured over $15 \text{ mm} \times 30 \text{ mm}$ surfaces using a laser profilometer with $0.05 \mu m$ of vertical resolution (Figures 10a, b and c at $Pc = 30$, 45 and 60 MPa respectively) and $\approx 20 \mu m$ of horizontal resolution. Note that due to a light contrast issue, surface elevation measurement failed for a fraction of the sampled surface at $Pc = 30$ MPa (indicated in light grey). Elevations range from about -25 to $25 \mu m$. At the lowest confining pressure we can observe coarse topographic highs (red colors) elongated in the direction of slip. These large and rough asperities likely correspond to gouge material accumulation with slip. The bigger one that we can see (at the bottom left) is about 2 mm thick, 5 mm long and $25 \mu m$ high. Compared to the other two experiments, no marker of the coseismic displacement is easily identifiable at $Pc = 60$ MPa, which is likely due to partial melting of the fault during rapid slip episodes. At the intermediate confining pressure $Pc = 45$ MPa, striations of the fault surface likely formed by mechanical abrasion have been preserved and reveal a flattened surface. At that scale it can clearly be seen that fault surfaces roughness at $Pc = 45$ MPa and $Pc = 60$ MPa are similar and less rough compared to the experiment conducted at $Pc = 30$ MPa.

We quantified fault surface roughness by means of the Hurst exponent H (also called roughness coefficient). To estimate H , we compute the Fourier power spectrum for each individual parallel profiles $I(k)$ perpendicularly and parallel to the slip direction as a function of the wavenumber k . Then we compute the average spectrum $P(k)$ (Figures 10d and e) of the whole surface in both directions (i.e., perpendicular and parallel to the slip direction) by stacking the individual Fourier transforms such as:

$$P(k) = \sum_{n=1}^{n=N} I_n(k) \quad (9)$$

where N is the total number of 1-D profiles. This ensures to lower the noise contained in 1-D individual profiles. For a self-affine 1-D profile, the Hurst exponent ranges between $0 \leq H \leq 1$ and $P(k)$ is related to H according to the following power law: $P(k) \propto k^{-1-2H}$. For a self-affine (i.e. fractal) 1-D profil, the roughness r will increase with the length of the profile l such as $r \propto l^H$.

A common feature to all the experiments is that fault surfaces roughness are similar both in terms of shape and amplitudes along the perpendicular and the parallel directions of sliding. This implies quasi-isotropic fault surfaces roughness and contrasts with what is observed in the case of natural faults. A large majority of natural faults are characterized by anisotropic self-affine surfaces (Candela et al., 2009). Although the Hurst exponents vary in the range [0.4 - 0.9], H is found to be around 0.6 along the direction of sliding, and around 0.8 in the direction perpendicular to the sliding direction. We may assume that the initially smooth fault surfaces in our experiments prevent fault surface roughness anisotropy from developing. Another possibility is that additional rapid slip episodes would have been required for fault surface roughness to become anisotropic. It is noteworthy that isotropic roughness also implies that gouge particles produced during slip are not only transported along the direction of slip but also perpendicular to it.

We found that for wavenumbers k less than $4 \times 10^3 \text{ m}^{-1}$ ($\approx 0.25 \text{ mm}$), fault surfaces roughness are characterized by a similar Hurst exponent H close to 0.4 which is rather low compared to what is typically found for natural fault but is a lower bound. A low Hurst exponent as opposed to a high Hurst exponent has the primary physical meaning that the ratio of roughness amplitude at long and short wavelengths is smaller which in the case of our experiments may be intrinsically related to fault surface preparation. The topography at long wavelength is necessarily damped to ensure an homogeneous contact between the two parts of the sample. However, to ensure a minimum of cohesion, fault surfaces are lapped with a fine-grained abrasive paper (#120 grit paper in this case, average particle diameter of about $125 \mu\text{m}$), which, in turns, produces small wavelength topography.

It can be clearly observed that fault surfaces roughness are nearly identical at $P_c = 45$ and $P_c = 60 \text{ MPa}$. Compared to the other two experiments, at $P_c = 30 \text{ MPa}$ the long wavelength roughness, inherited from gouge particles accumulation, emerges for wavenumbers k less than about $4 \times 10^3 \text{ m}^{-1}$ ($\approx 0.25 \text{ mm}$). It can be clearly observed that Fourier power spectra of fault surfaces topography share significant similarities with AEs G-R distribution. For moment magnitudes M_w larger than about -7.6, the G-R slope rapidly drops at $P_c = 45 \text{ MPa}$ and $P_c = 60 \text{ MPa}$ but is unchanged at $P_c = 30 \text{ MPa}$. This could be the reciprocal of the decrease in roughness amplitudes for wavelengths higher than about 0.25 mm ($k \approx 4 \times 10^3 \text{ m}^{-1}$) observed at $P_c = 45 \text{ MPa}$ and $P_c = 60 \text{ MPa}$. We can speculate onto the fact that AEs G-R distribution mirrors fault surface roughness. This is intriguing but would require more quantitative analysis to be validated.

4 Statistics of the nucleation phase

4.1 Evolution of precursory AE activity towards nucleation

Figures 11a, b and c display the cumulative AE moment release and the temporal variations of b-value as a function of normalized time to failure at $P_c = 30 \text{ MPa}$, $P_c = 45 \text{ MPa}$ and $P_c = 60 \text{ MPa}$ respectively. Note that for each experiment, all AE sequences were stacked. b-values were estimated for three different time intervals which were selected in order to contain a similar number of AEs. To ensure that no bias would be introduced due to AEs saturation, b-values were computed either by taking into account all AEs (diamond symbols) or by removing AEs with $M_w > -7$ (square symbols). Including or not the AEs that have saturated impacts only the absolute value of b but not its temporal variation.

Hereafter, we discuss on b-value variations for the complete AE catalogs (i.e. that includes all magnitudes). At $P_c = 30 \text{ MPa}$ we estimate that the b-value is about 0.68 ± 0.02 up to (on average) ≈ 3 seconds prior to failure. Then the b-value drops rapidly to an almost constant level: 0.49 ± 0.02 and 0.52 ± 0.02 . At $P_c = 45 \text{ MPa}$ the b-value is close to 0.7 ± 0.04 up to ≈ 2.5 s prior to failure and then drops to 0.54 ± 0.04

and 0.59 ± 0.04 . For both experiments, b-value increases slightly in the last tenths of a second but this lies into the range of uncertainties. b-value temporal variations prior to failure are more complicated to analyse for the experiment conducted at $Pc = 60$ *MPa* for two reasons (i) the large uncertainties and (ii) about 90 % of the AEs were recorded in the last 3 seconds prior to failure which lowers considerably the temporal resolution of b-value variations during stick-slip cycles. In comparison about 30 % and 25% of the total number of AEs were generated before entering the last 3 seconds prior to failure at $Pc = 30$ and $Pc = 45$ *MPa* respectively. However, unlike the other two experiments the b-value is initially low, close to 0.61 ± 0.06 . In the last second prior to failure the b-value returns to a fairly high value, about 0.76 ± 0.08 and then decreases again to 0.67 ± 0.05 .

Temporal variation in b-value prior to failure has been well documented during fracture experiments conducted on intact rock samples (Scholz, 1968b) and during rock friction experiments (Goebel et al., 2012; Kwiatek et al., 2014; Rivière et al., 2018). Fracture experiments on intact samples show that b-value and differential stress are anticorrelated, which takes its origin in the formation and the coalescence of microfractures. Such a process causes a large number of AEs to be generated and a smooth and accelerating drop of b-value up to the time of failure. Decrease in b-value towards failure has also been documented preceding large subduction earthquakes (Suyehiro, 1966; Enescu & Ito, 2001; Nanjo et al., 2012; Tormann et al., 2015). However, foreshocks that precede large earthquakes occur on time scales from hours to years. Long term variations of b-value are usually attributed to stress accumulation or partial stress release while short term variations are related to the mainshock nucleation. Based on the two experiments conducted at $Pc = 30$ *MPa* and $Pc = 45$ *MPa* we can at least say that large AEs rapidly grow in the last seconds preceding failure. The rapid drop of b-value prior to stick-slip instabilities better suggests rapid weakening of the fault interface in a short interval of time close to failure.

4.2 Precursory AEs dynamics and fault maturation

Figures 12a ,b and c compare the along fault displacement, the along fault velocity, the cumulative number of AEs and the cumulative AE moment release with respect to time to failure at $Pc = 30$ *MPa*, $Pc = 45$ *MPa* and $Pc = 60$ *MPa* respectively. Each quantity is normalized by its maximum value at the time of failure. Here again, all AE sequences are stacked to bring out a general trend. The grey shaded area indicates the range of uncertainty for the cumulative AE moment release. Figures 12d, e and f show the cumulative precursory AE activity per SSE at $Pc = 30$ *MPa*, $Pc = 45$ *MPa* and $Pc = 60$ *MPa* respectively . Cumulative precursory AE activity is normalized by its final value and is plotted against normalized time to failure. The colorscale refers to the SSE index and the black curves result from the stacking of all AE sequences. Note that for visual inspection, not all AE sequences are shown at $Pc = 30$ *MPa* (Figure 12d) and at $Pc = 45$ *MPa* (Figure 12e).

Consistently with previous experimental studies (McLaskey & Lockner, 2014; Passelègue et al., 2017), we have always observed that the displacement onto the fault accelerates preceding failure. However, although along fault slip is required to generate AEs, both the number of AEs and the AE moment rather appear to correlate with the slip rate onto the fault. This is particularly well illustrated in the last seconds prior to failure during which AE moment release and along fault slip velocity almost collapse. Nevertheless, there are notable differences between the experiments, both in terms of AE moment release and mechanical behavior of fault surfaces. The cumulative AE moment release exhibits the smoothest behavior at $Pc = 30$ *MPa*. Seismic energy is continuously radiated from the fault but in a delayed fashion with respect to the slip rate. For instance, between about -15 s and -5 s, the slip rate linearly increases with time while the AE moment release remains low. These features can be retrieved for the experiments conducted at $Pc = 45$ *MPa*. The AE moment release follows the fault slip

rate but is delayed and starts to intensify only once the fault accelerates. In the same way than the experiment conducted at $P_c = 30 \text{ MPa}$, the slip rate increases linearly before accelerating (between about -5 and -2 s prior to failure). However, compared to the experiment conducted at $P_c = 30 \text{ MPa}$, the slip rate onto the fault and the AE moment release increase later prior to stick-slip instabilities and at higher rate. The picture depicted by the experiment conducted at $P_c = 60 \text{ MPa}$ is somewhat different. Although we observe a clear correlation between the fault slip velocity and the AE moment release, the seismic energy is not released continuously, but rather in bursts. For instance, the two largest AEs that were recorded ($M_w > -6.9$) occurred about -17 s and -5 s prior to failure, while the fault had not accelerated yet. This case is not limited to the experiment conducted at $P_c = 60 \text{ MPa}$ and also occurred at $P_c = 30 \text{ MPa}$ and $P_c = 45 \text{ MPa}$. Even at the small scale of the experiments presented here, stress and thus strain are not homogeneously released during coseismic displacement. Bursts of AE activity that occur without external forcing such as slip acceleration might reflect the brittle failure of small patches where residual stress accumulated. Also, the stacking procedure inherently smooths the variability of precursory AE sequences. It is likely that bursts of AE activity would have been smoothed if a larger number of AE sequences would have been stacked together at $P_c = 60 \text{ MPa}$.

AEs may reflect the brittle destruction of fault surface topography or may occur when stress applied onto the fault exceeds the strength of local brittle fault patches. For sufficiently large AEs ($M_w > -8.6$) we often observed positive and negative first P-wave arrivals which implies that most of the moment release is deviatoric. According to the similarity between fault slip velocity and cumulative AE moment release, we posit that precursory AEs highlight the rupture of locked portions of the fault embedded in and loaded by an aseismically slipping larger portion. Similar observations have been reported in larger scale experiments (McLaskey & Kilgore, 2013). This is also consistent with observations at the scale of crustal faults. Bouchon et al. (2013) showed that foreshock sequences were more common for interplate than for intraplate earthquakes due to facilitating slow slip phase at plate boundaries. Similarly, McGuire et al. (2005) have observed that oceanic transform faults with relatively high-slip rates were producing more foreshock sequences. However, the susceptibility of a fault to produce foreshocks will depend at first order of its degree of heterogeneity.

The experiment conducted at $P_c = 30 \text{ MPa}$ gives the clearest example of what we would call "fault maturation" (Figure 12d). At the early stage of the experiment, most of the AE activity remain concentrated close to failure, but with the successive ruptures, precursory AE activity increases in number and occurs earlier during loading. Summing all AE sequences results in a smooth increase of the cumulative number of AEs as previously described. These characteristics can be approximately retrieved at the intermediate confining pressure, $P_c = 45 \text{ MPa}$ (Figure 12e) but not at $P_c = 60 \text{ MPa}$ (Figure 12f). During this experiment, AEs occur later which results in a sharper acceleration of the cumulative number of AEs towards failure. A noticeable difference at $P_c = 60 \text{ MPa}$ lies in the absence of AEs early during loading. On the other hand, the experiment conducted at $P_c = 60 \text{ MPa}$ is the only one for which the first sequence of AEs has released a comparable amount of seismic energy with respect to the ones that followed. At $P_c = 30 \text{ MPa}$ and $P_c = 45 \text{ MPa}$, the AE moment release prior to failure started to significantly increase after 10 stick-slip cycles. However, when averaging over all AE sequences, the experiments conducted at $P_c = 45 \text{ MPa}$ and $P_c = 60 \text{ MPa}$ are characterized by a similar AE frequency-magnitude distribution. Conversely, significantly more large AEs were generated during the experiment conducted at $P_c = 30 \text{ MPa}$. In the following, we attempt to rely on microstructural and fault surface roughness analysis to explain the similarities and differences of AE timing and moment release.

Fault strength heterogeneity arises, in part, from multiscale roughness and spatial variations of fault rheology. Compared to the other two experiments, large asperities were formed by mechanical abrasion of the fault surface at $P_c = 30 \text{ MPa}$ which

increased the level of fault strength heterogeneity in terms of stress concentration and frictional resistance and which, consequently, provided the necessary conditions to generate large AEs. At $P_c = 45 \text{ MPa}$ and $P_c = 60 \text{ MPa}$, same fault surface roughness produce similar AEs. We can argue that fault surfaces were more scrubbed at $P_c = 45 \text{ MPa}$ and $P_c = 60 \text{ MPa}$ because of either thermally activated plastic deformation processes or partial melting. It is noteworthy that for the experiments conducted at $P_c = 45 \text{ MPa}$ and $P_c = 60 \text{ MPa}$ the average amount of pre-slip was quite similar (about $9 \mu\text{m}$) and larger than the one for the experiment conducted at $P_c = 30 \text{ MPa}$ (about $6 \mu\text{m}$). This is probably caused by the organized large scale roughness resisting slip (Schaff et al., 2002) that has developed at $P_c = 30 \text{ MPa}$.

However, almost no large AEs were produced at the early stage of the experiments conducted at $P_c = 30 \text{ MPa}$ and $P_c = 45 \text{ MPa}$. Let us take a step back to the mechanical data. At $P_c = 30 \text{ MPa}$ and $P_c = 45 \text{ MPa}$, the first SSE happened at particularly low stress conditions, when the average normal stress σ_n onto the fault was about 43 MPa and 65 MPa respectively resulting in coseismic displacements of $31 \mu\text{m}$ and $59 \mu\text{m}$. In comparison, at $P_c = 60 \text{ MPa}$ the first SSE occurred when the normal stress acting onto the fault was about 98 MPa resulting in a coseismic displacement of $184 \mu\text{m}$. Slip during the first SSE at $P_c = 60 \text{ MPa}$ probably produced fine gouge or accentuated topographic heterogeneities that effectively increased the roughness and promoted the generation of relatively large AEs prior to the subsequent SSE. Therefore, the fault was already "mature". At the other two confining pressure conditions, more SSEs were required to increase the roughness due to smaller coseismic displacements and lower normal stress conditions. Once a sufficient amount of gouge particles or topographic heterogeneities were produced, both the number of AEs and the AE moment release started to intensify.

Finally, the absence of AEs far from failure at $P_c = 60 \text{ MPa}$ may be related to the spatial distribution of gouge particles and their interactions with the underlying surface. AEs that happen early during loading are considerably small, which causes the high b-values far from failure at $P_c = 30 \text{ MPa}$ and $P_c = 45 \text{ MPa}$. We interpret these small AEs as either micro-shear events or buckling of a force chain in a compacted gouge layer (Mair et al., 2002; Hartley & Behringer, 2003). Thus, these small AEs cannot be generated at $P_c = 60 \text{ MPa}$ because of either the homogeneous distribution of gouge particles onto the fault or due to the fact that a significant fraction of gouge particles is trapped into the melt. However, another possibility is that small AEs that happen early during loading at $P_c = 30 \text{ MPa}$ and $P_c = 45 \text{ MPa}$ reflect microfracturing processes promoted by the damage accumulation with cumulative slip.

4.3 Spatial distribution of precursory AEs

Here we look at the evolution of the precursory AEs spatial distribution towards failure. In what follows, "nucleation" refers to the location on the fault surface where SSEs initiated and was estimated according to first p-wave arrivals. SSEs whose nucleation sites were poorly constrained (less than about $2\text{-}3 \text{ mm}$) are not shown here. Figures 13a, b and c display the distance to nucleation (i.e. where SSEs initiated) of the precursory AEs as a function of normalized time to failure at $P_c = 30 \text{ MPa}$, $P_c = 45 \text{ MPa}$ and $P_c = 60 \text{ MPa}$ respectively. Cyan triangles indicate the average distance to nucleation and its standard deviation computed into 10 evenly log-distributed time bins. To the left is displayed the AEs distribution as a function of distance to nucleation. Note that, AEs located with more than $0.3 \mu\text{s}$ travel time residuals (about $2\text{-}3 \text{ mm}$ of location accuracy) were disregarded. At the lowest confining pressure, $P_c = 30 \text{ MPa}$, nothing indicates on spatial migration of the precursory AEs towards nucleation. Precursory AEs remain randomly distributed over the fault surface up to the time of failure. Most of the precursory AEs occurred at larger distances than 20 mm relative to where SSEs initiated. However, the randomness of AEs spatial distribution tends to decrease with increasing stress conditions. At the highest confining

pressure, $P_c = 60 \text{ MPa}$, the majority of the AEs occurred on a more localized portion of the fault surface, within 10 to 15 mm relative to where SSEs initiated. In that case, precursory AEs do not occur randomly on the fault surface but migrate, on average, towards where SSEs initiated.

The precursory AEs spatial distribution yields relevant information about the way SSEs initiate. In all experiments, we found that SSEs are always preceded by preslip acceleration phase and that preslip drives smaller scale seismicity (i.e. AEs). As proposed by McLaskey and Lockner (2014), preslip may sufficiently weaken fault strength to facilitate a small instability to grow large and eventually propagate over the entire fault. In such a scenario, precursory AE activity in the last milliseconds prior to failure should co-localize with locations where SSEs initiated. This would result in clear migration patterns (Figure 13), which is not what we observe. In our experiments, we found that SSEs do not necessarily nucleate where precursory AE activity concentrates but rather at the edges of the areas where most of the precursory AE moment was released. This is well illustrated for the last SSEs at $P_c = 30 \text{ MPa}$ and $P_c = 45 \text{ MPa}$ (Figure 8). Moreover, we would expect that large precursory AEs promote cascade process. While the largest AEs were generated at $P_c = 30 \text{ MPa}$, there is no indication of migration over time for this experiment. Therefore, our observations better suggest that, in most cases, SSEs begin as slowly growing fault slip that transitions to dynamic rupture rather than resulting from a small AE that would propagate over the entire fault in a cascade-up process.

We attempt here to give a qualitative explanation for migration patterns promoted by increasing stress conditions. We may assume that if the nucleation length L_c is smaller, there is more chance that precursory AEs occur at shorter distances to where SSEs initiate, which would, consequently, favor migration. According to slip weakening linear (Ida, 1972; Campillo & Ionescu, 1997; Uenishi & Rice, 2003) or rate-and-state friction (R&S) laws (Rubin & Ampuero, 2005; Ampuero & Rubin, 2008) we expect the critical nucleation length L_c to decrease with increasing the normal stress acting onto the fault such as:

$$L_c = 2 \cdot \beta \cdot \frac{\mu D_c}{\sigma_n (f_s - f_d)} \quad (10)$$

for the linear slip weakening law where μ is the shear modulus of the rock sample, D_c is the critical slip distance, σ_n is the normal stress acting onto the fault, f_s and f_d are the static and the dynamic friction coefficients respectively and β is a non-dimensional shape factor coefficient (≈ 1.158). For R&S friction laws:

$$L_c = \frac{\mu D_c}{\sigma_n (b - a)} \quad (11)$$

where b and a are the constitutive parameters of R&S friction laws. According to (10) and (11), L_c will decrease with increasing the normal stress acting onto the fault and the friction drop. However, D_c is expected to increase with increasing the normal stress acting onto the fault. For instance, assuming a purely slip weakening behavior, D_c is expressed as (Ida, 1972; Palmer & Rice, 1973; Rice, 1979):

$$D_c = \frac{16(1 - \nu) V_r t_w \sigma_n (f_s - f_d)}{16\pi \mu} \quad (12)$$

where V_r is the local rupture velocity, t_w is the weakening time and ν is the poisson's ratio of the rock specimen. D_c is also expected to increase with normal stress and friction drop. Moreover, while weakening time t_w does not vary much with stress conditions (Passelegue et al., 2016), we expect that rupture velocity will, on

average, increase with normal stress. Therefore, we do not necessarily expect that L_c decreases with increasing σ_n .

One possible explanation may lie into stress heterogeneity. Let us assume that the nucleation zone expands in a crack-like fashion. Inside the crack, the shear-stress drop $\Delta\tau$ can be approximated as the shear modulus μ of the medium times the ratio between the slip velocity V_s and the shear-wave velocity C_s such as:

$$\Delta\tau = -\mu \frac{V_s}{C_s} \quad (13)$$

In the case of an expanding crack, the slip velocity is maximum at the tips and nearly uniform inside the crack. As the nucleation zone expands, unlocked portions of the fault in the interior of the nucleation zone releases stress. Due to stress perturbations close to the tips of the nucleation zone, the stress-drop $\Delta\tau$ is positive near the tips and decreases and becomes negative in direction of the center of the nucleation zone. However, this is only valid for areas in the interior of the nucleation zone that are able to slip. Locked portions of the fault inside the nucleation zone continuously accumulate stress, even after nucleation started. In that case, the stress-drop $\Delta\tau$ is positive near the tips and decreases but remains positive in direction of the center of the nucleation zone.

Let us propose the following mechanism to explain the correlation between increasing stress conditions and precursory AEs migration: AEs may occur if the applied stress to a locally brittle patch exceeds its strength. Precursory AEs at relatively large distances from the center of the nucleation zone are triggered first due to stress perturbations at the tips of the nucleation zone, which are sufficient to overcome the critical strength of the locked portions of the fault interface. As the nucleation zone expands, stress build-up in the interior of the nucleation zone. Because of the negative gradient of the stress profile that goes from the edges of the nucleation zone to its center, the precursory AEs will tend to migrate towards the center of the nucleation zone. This mechanism is schematically presented in figure 14d. As an illustration, the figures 14a, b and c display a summary of the precursory AEs sequence prior to SSE #6 at $Pc = 60MPa$. The cumulative AE moment release and along fault displacement in the last 10 seconds prior to failure are shown in figure 14a. Figure 14b displays the distance to nucleation of the precursory AEs as a function of time to failure and the figure 14c shows the locations on the fault plane of the precursory AEs. The colorscale refers to the occurrence time of the precursory AEs relative to failure and the star symbol indicates where the SSE initiated. This precursory AEs sequence is characterized by three bursts of microseismicity which occurred about -2.2, -0.5 and -0.1 s prior to failure (Figure 14a). The AE moment release rapidly increased in the same way that the displacement onto the fault which is consistent with the interpretations made so far (i.e., AEs highlight the rupture of brittle fault patches within the interior of the nucleation zone). In that case, AEs migration is clearly identifiable. Initially, precursory AEs locate at about 20-25 mm from where the SSE initiated and then rapidly migrate towards the latter (Figure 14b). To be fully consistent with the interpretation proposed above, the edges of the nucleation zone were close to the locations of the first burst of microseismicity that occurred about -2.2 s prior to failure (Figure 14c). In the case of a self-similar crack, we expect that the displacement in the interior of the nucleation zone grows as the nucleation zone expands. According to the displacement along the fault, we can assume that the nucleation zone has then rapidly expanded after -2.2 s prior to failure. This resulted into the fast loading of the locked portions of the fault which triggered the subsequent bursts of microseismicity. AEs migration was then controlled by the shear-stress gradient in the interior of the nucleation zone. In such a scenario, fault strength homogeneity will favor migration, while fault strength heterogeneity will make precursory AE activity to randomly occur relative to the center of the nucleation zone. Assuming that fault strength heterogeneity is, at first order,

provided by multiscale roughness of the fault plane, this may explain why migration is not observed at the lowest confining pressure $P_c = 30 \text{ MPa}$ but only emerges when increasing normal stress. It should also be noted that AEs may also be able to trigger each other due to dynamic or static stress transfer. In that case, we would expect them to draw a well defined path, both in time and space, which is not what we observe. Therefore, this may happen but is likely of second order.

Foreshock migration prior to large earthquakes is often attributed to slow-slip propagation towards the mainshock hypocenter (Kato et al., 2012; Ruiz et al., 2014; Kato & Nakagawa, 2014). It has also been suggested that fluids diffusion may trigger foreshock swarms by reducing effective normal stress (Moreno et al., 2015; Socquet et al., 2017). The experiments were conducted under dry conditions which makes the latter case unlikely. Slow slip transients usually involve slip rates that range from 10 to 100 $\mu\text{m/s}$. This is more than what we observe during our experiments, fault slip rates are typically of the order of few $\mu\text{m/s}$ in the last tenth of a second prior to failure. The question whether slow slip transients prior to large earthquakes are part of the nucleation process or not is still debated. The 2014 M_w 8.2 Iquique and the 2011 M_w 9.0 Tohoku-oki earthquakes were both preceded by slow slip events, however the latter did not propagate with slip (and foreshock rate) acceleration which is kinematically expected in case of nucleation process. Therefore, slow-slip transients were not interpreted as part of the nucleation process. This contrasts with the case of the 1999 M_w 7.6 Izmit earthquake prior to which an increase in seismicity rate (including repeaters) and seismicity migration towards the mainshock hypocenter were reported (Bouchon et al., 2011). We have attempted to give a qualitative interpretation of AEs migration during our experiments. This may also be a plausible explanation for foreshock migration prior to natural earthquakes. In such a case, there is no need to involve fluids diffusion or slow-slip propagation.

4.4 Temporal distribution of foreshocks

Here we look at the temporal evolution of the cumulative number of precursory AEs prior to failure. When averaged over numerous foreshock sequences, it is known that the foreshock rate $N(t)$ increases as an inverse power law of the time to the mainshock (L. M. Jones & Molnar, 1979) such as:

$$N(t) = \frac{K}{(c + \Delta t)^p} \quad (14)$$

where K is the foreshock productivity, c and p are empirical constants and Δt is the time that separates from the mainshock. A previous experimental study (Passelègue et al., 2017) showed that AE activity was increasing exponentially towards failure which has been interpreted as a consequence of preslip which is itself exponential. In our experiments, we found that precursory AE activity better follows an inverse power law of time of the form of (14). Figures 14a, b and c show the cumulative number of AEs $N_a(t)$ in the last 35 seconds prior to failure at $P_c = 30 \text{ MPa}$, $P_c = 45 \text{ MPa}$ and $P_c = 60 \text{ MPa}$ respectively. The cumulative number of AEs results from the stacking of all AE sequences and is averaged over all sequences. This allows us to conserve the smooth shape of the cumulative total number of AEs and to compare between the experiments the average number of precursory AEs during individual sequence. Thus we can express $N_a(t)$ as:

$$N_a(t) = \frac{K}{(c + \Delta t)^p} \quad (15)$$

where Δt is the time to failure which is positive in that case. The red curves display the best fits that we obtained over the parameters c and p . The parameters p

and c were searched in the range [0.1-3] with a step of 0.01. We made the choice to link K to c and p such as $K = N_f \cdot (c^p)$ where N_f is the average cumulative number of AEs at the time of failure. This ensures that the average cumulative number of AEs at the time of failure equals N_f . The logarithm of the residuals is given by the inserted panels as a function of p and c . Residuals are normalized by the minimum (i.e., the value 0 indicates minimum). The best fits were obtained for $c = 2.39 \pm 0.3$ s and $p = 1.31 \pm 0.08$, $c = 0.6 \pm 0.25$ s and $p = 0.79 \pm 0.1$ and $c = 0.24 \pm 0.09$ s and $p = 0.82 \pm 0.05$ at $Pc = 30$ MPa, $Pc = 45$ MPa and $Pc = 60$ MPa respectively. Uncertainties correspond to the 90 % confidence level. The average AEs rate is given by the time derivative of (15) such as:

$$\dot{N}_a(t) = -K \frac{p(c + \Delta t)^{p-1}}{(c + \Delta t)^{2p}} \quad (16)$$

which gives:

$$\dot{N}_a(t) = -K \frac{p}{(c + \Delta t)^{p+1}} \quad (17)$$

As we could have expected, the power exponent p is higher for the average AE rate. If we use the best values of p that we estimated, we obtained $p = 2.31$, $p = 1.79$ and $p = 1.82$ at $Pc = 30$ MPa, $Pc = 45$ MPa and $Pc = 60$ MPa respectively. This values are larger than the typical values found for tectonic seismicity which are less or close to unity (Helmstetter & Sornette, 2003b). It should be noted that we have linked K to c and p which may affect the results. Indeed, the three parameters K , c and p are linked to each other. The most common way to estimate them is to use the maximum likelihood method (Ogata, 1983). However, since we have linked K to c and p in the same way for each experiment and that N_f do not differ much (N_f equals 17, 13 and 14 at $Pc = 30$ MPa, $Pc = 45$ MPa and $Pc = 60$ MPa respectively) we believe that the results obtained can be compared relative to each other. Most of the time, the seismicity rate, whether it is for foreshocks or aftershocks, is only related to the parameter p . The physical meaning of c received far less attention while both will impact the seismicity rate. A decrease of c or an increase of p will result in a higher seismicity rate. At the laboratory scale, it has been demonstrated that p correlates with strain rate (Ojala et al., 2004) and with stress heterogeneity in the context of rate and state friction law (Dieterich, 1994). This would be consistent with the high value of p that we found at $Pc = 30$ MPa compared with the other two experiments since the fault surface presented higher roughness for this experiment (i.e. higher stress heterogeneity). The parameter c may control in a sense when microseismicity starts. We can assume that precursory seismicity/AE activity may start at earlier time in case of an heterogeneous medium. This will have a counter effect on seismicity rate since brittle failures of locked areas of the fault will be more diffuse in time. In that case the parameter c will increase and seismicity rate will decrease. This may explain why we found an higher value of c at $Pc = 30$ MPa. However, this is only speculation and would require further analysis and additional data to be validated.

According to (17) and using the best set of parameters obtained for c and p , we find that the average AE rate is about 5 times larger at $Pc = 60$ MPa compared with $Pc = 30$ MPa and about two times larger at $Pc = 45$ MPa compared with $Pc = 30$ MPa at the time of failure. This correlates well with the fault velocity. If we compare with the average fault slip velocity in the last millisecond we find that the fault slip rate is about four times larger at $Pc = 60$ MPa (about 4 $\mu\text{m/s}$) compared with $Pc = 30$ MPa and about three times larger at $Pc = 45$ MPa compared with $Pc = 30$ MPa. Given the good correlation that we found between along fault velocity and AE cumulative number (Figure 12), we suggest that AE rate is primarily controlled by

fault slip rate. However, it should be noted that this is only valid on average since precursory AE sequences exhibit variable behaviors with respect to each other.

5 Scaling laws and implication to natural faults

5.1 AE source parameters

Numerous studies show that the scaling relationship between moment magnitude and corner frequency $M_0 \propto f_c^3$ is verified whether for earthquakes at the scale of crustal faults, induced seismicity or laboratory generated AEs, that is for a wide range of moment magnitudes from -8 to 8. (Aki, 1967; Abercrombie, 1995; Hiramatsu et al., 2002; Prieto et al., 2004; Yamada et al., 2007; Kwiatek et al., 2011; Yoshimitsu et al., 2014). Demonstrating that laboratory generated AEs satisfy the scaling relationship between moment magnitude and corner frequency is crucial since it allows valuable inferences to be drawn about whether or not knowledge obtained in the laboratory can be extrapolated to the natural field. Figures 16a, b and c display the corner frequencies f_c versus the seismic moments M_0 and moment magnitudes M_w obtained by inversion for the recorded AEs at $Pc = 30 \text{ MPa}$, $Pc = 45 \text{ MPa}$ and $Pc = 60 \text{ MPa}$ respectively. Errorbars for the estimated corner frequencies and moment magnitudes are indicated in light gray. We recall that we could not estimate f_c for the AEs with moment magnitudes less than $M_w = -8.6$ due to too low signal to noise ratio neither for the AEs with $M_w > -7$ due to the saturation of the acoustic sensors. Figure 16d shows the comparison between the AEs source parameters and a corpus of other studies which gathers natural earthquakes and laboratory generated AEs having moment magnitudes of -4 to 4. Figure 16d was re-adapted from the study of Yoshimitsu et al. (2014) but note that data from the study of Yoshimitsu et al. (2014) do not appear on figure 16d since they overlap with ours.

According to the expected scaling relationship between M_0 and f_c we find no differences between the AEs recorded during our experiments and natural earthquakes. AEs have corner frequencies that mostly range from 300 kHz (source size $\approx 4 \text{ mm}$) to 1.5 MHz (source size $\approx 0.5 \text{ mm}$). The average stress-drops we obtained are 1 MPa, 0.88 MPa and 0.68 MPa at respectively $Pc = 30 \text{ MPa}$, $Pc = 45 \text{ MPa}$ and $Pc = 60 \text{ MPa}$. Quite surprisingly, we find that larger AEs have larger stress-drops. This might be directly related to insufficiently well calibrated acoustic sensors. Using ball drop momentum transfer for acoustic sensors calibration, McLaskey et al. (2015) showed that the peaks of resonance that characterize the instrumental response of an acoustic sensor were diminished under confinement. Because the acoustic sensors were calibrated under atmospheric pressure, it is possible that particular frequency bands were overdamped. Thus, corner frequencies, near these frequency bands would be underestimated. Another possibility is that the length of the time window that we used (50 μs centered on the theoretical first S-wave arrival) to compute the spectra was too long to sufficiently reduce the energy coming from surface waves. Surface waves carry high-frequency energy which, thus, will be contained into the spectra. As we expect surface waves to be less attenuated for larger AEs this would be consistent with overestimated corner frequencies for the largest AEs. However, this feature might also be physically meaningful. Large AEs tend to occur closer to stick-slip instability when stressing rate is higher due to accelerating aseismic slip which will thus result in larger stress-drops in case of larger AEs.

According to the seismological parameters estimated for the AEs, we infer that the latter can be considered as micro-earthquakes. In a sense, AEs might be more similar to natural earthquakes than SSEs are since they highlight self-terminating ruptures that are contained in an elastic material with similar mechanical properties.

5.2 Pre-seismic moment and coupling

We inferred that SSEs initiated as the expansion of an aseismically slipping fault patch that was driving precursory AE activity. Figure 17a compares the total AE moment release per SSE M_a with the pre-seismic moment release M_p . Note that we report here only the precursory AE sequences that do not include saturated AEs which equates to 67 SSEs out of 97. Figure 17b shows pre-seismic moment release as a function of co-seismic moment release. Our data (diamond symbols) are plotted together with the observations made by two previous experimental studies ((Passelegue et al., 2017; Acosta et al., 2019), grey symbols). The inserted figure displays the comparison between our observations and what was found for a set of large earthquakes. These earthquakes are the 1999 M_w 7.6 Izmit earthquake (Bouchon et al., 2011), the 2011 M_w 9.0 Tohoku-Oki earthquake (Kato et al., 2012), the 2012 M_w 7.6 Nicoya earthquake (Voss et al., 2018), the 2014 M_w 8.2 Iquique earthquake (Socquet et al., 2017) and the 2015 M_w 8.4 Illapel earthquake (Huang & Meng, 2018). Pre-seismic moment release and co-seismic moment release were estimated according to $M_{p,c} = \mu D_{p,c} S$ with μ being the metagabbro shear modulus ($\mu = 40 \text{ GPa}$), S the surface of the fault and D_p and D_s the pre-seismic slip and the co-seismic slip respectively. D_p is to the total macroscopic fault slip from the beginning to the end of loading and thus includes preslip related with nucleation and potential creep. In addition, the size of the nucleation zone might be smaller than the total surface of the fault which implies that M_p constitutes an upper bound.

The total AE moment release prior to nucleation represents only a very small percentage of the pre-seismic slip (Figure 17a). The ratio between both, that we refer as to "seismic coupling" hereafter, ranges from about $5 \cdot 10^{-7}$ ($5 \cdot 10^{-5}\%$) to $4 \cdot 10^{-4}$ (0.04 %). Such a low seismic coupling may explain why, in our experiments, SSEs are unlikely to result from a cascade process. Indeed, we can assume that cascading failure processes require the rupture of patches large enough to propagate over the entire fault. However and without a doubt, the precursory AE sequences that include saturated AEs imply higher seismic coupling. The largest number of oversaturated ($M_w > 6.8$) AEs was generated prior to SSE #53 at $Pc = 30 \text{ MPa}$. Let us assume a drastic scenario in which all of them would have been $M_w \approx 6.0$ AEs. Even in that hypothetical case, we estimate that the seismic coupling would be still low, of the order of 0.2%.

Plotting the total AE moment release M_a as a function of the pre-seismic moment M_p indicates that M_a goes as M_p^4 . In the case of an isotropic expansion of a circular crack with length L the moment release inside the crack would scale as $\Delta\tau L^3$ (Madariaga, 1976). For a self-similar crack, the amount slip D inside the crack scales with its length L . Therefore, by making the approximation that the nucleation zone expands in the same way that a self-similar circular crack, we could have expected that M_a goes as M_p^3 . The fact that M_a scales as M_p^4 can be explained if AEs have stress-drops that are magnitude dependent, that is higher stress-drops for larger magnitudes, which would be consistent with the AEs source parameters that we obtained (Figure 16). Note that extending this scaling relationship to larger pre-seismic moments would rapidly lead to 100 % of coupling. Taking the experiment conducted at $Pc = 45 \text{ MPa}$, as an example, M_a would equal M_p for $M_p \approx 10^{4.5} \text{ N.m}$. $M_p \approx 10^{4.5} \text{ N.m}$ equates an amount of pre-slip of about $300 \mu\text{m}$. If we consider a ratio of M_p/M_c of about 5% this implies a co-seismic slip displacement of about 6 mm . Assuming a linear scaling between the co-seismic displacement and the rupture length, 6 mm of coseismic slip is expected for an earthquake of magnitude M_w about 2.5-3. A recent study (Tamaribuchi et al., 2018) investigated foreshock activity characteristics using the JMA catalog over the last 20 years. Despite the fact that the magnitude of the largest foreshock within a sequence scales with the magnitude of the mainshock, it has been observed that many mainshocks are not preceded by foreshock activity, at least not by foreshocks of $M_w > 1.0$ (the completeness magnitude of the catalog). Moreover, there are numerous foreshock sequences associated with mainshocks

of magnitude $M_w \geq 2.5$ for which the magnitude of the largest foreshock is at least 2 orders of moment magnitude less than that of the mainshock. If 100 % of coupling was consistently expected during nucleation, we would expect to observe very often intense foreshock activity. One possibility is that the power law 4 that we find between M_a and M_p is related to the experimental conditions such as rapid loading which likely prevents healing, the smoothness of the fault which may promote pre-slip or its simple geometry which could favor smooth acceleration of the fault plane during nucleation.

In a recent study, Acosta et al. (Acosta et al., 2019) argued that the pre-seismic moment release M_p should scale with the co-seismic moment release M_c . This scaling relationship is expected if fracture energy increases as a power law of co-seismic displacement (Abercrombie & Rice, 2005; Ohnaka, 2013; Passelègue et al., 2016) such as:

$$G = au_{cos}^\alpha \quad (18)$$

where a is a scaling pre-factor and α is a given power and u_{cos} is the co-seismic displacement. The following empirical scaling relation between M_p and M_c was proposed (indicated by the slope=0.56, figure 17b):

$$M_p \propto M_c^{0.56} \quad (19)$$

On average, M_p contribute to about 4 %, 6 % and 2 % of M_c at $Pc = 30$ MPa, $Pc = 45$ MPa and $Pc = 60$ MPa respectively. This is slightly less than what was found by Passelègue et al. (2016) and Acosta et al. (2019) but is typically of the same order of magnitude. If we only look at the experimental data (Figure 17b), it is hard to distinguish if M_p scales as $M_c^{0.56}$. Experimental observations may also simply indicate a linear relation between M_p and M_c as given by the slope of 1. Although the nucleation phase can not be appropriately examined through geodetic measurements for most earthquakes (either because of a lack of instrumentation or because of low earthquake magnitudes), well instrumented large interplate earthquakes form exceptions. Excepted for the 1999 M_w 7.6 Izmit earthquakes, the examples that we show in figure 17b have M_p/M_c that ranges from about 0.4 % to 3 %. All those earthquakes have in common that their precursory moment was estimated using geodetic and/or repeater measurements. The precursory moment associated with the M_w 7.6 Izmit earthquake was inferred (Bouchon et al., 2011) only from repeaters and was about 6 orders of magnitude lower than the co-seismic moment. It is likely that the occurrence of repeaters in a short amount of time requires a fast reloading of stress. This is typically what is expected during nucleation since slip is accelerating up to dynamic rupture. However, our observations suggest that coupling may be extremely low during nucleation. Therefore, only relying on the seismic moment released by repeaters may result in a lower bound estimation of M_p if a significant part of the precursory slip is accommodated aseismically. Comparing our results with what is typically observed for large interplate earthquakes, it suggests a simple linear relation between M_p and M_c (Figure 17b). This would imply that fracture energy is proportional to co-seismic displacement. Note that different forms of (19) were proposed. For instance, within the framework of slip-weakening theory and on the basis of seismological observations, Abercrombie and Rice (2005) proposed that $M_p \propto M_c^{0.78}$.

Comparing the total AE moment release M_a with the co-seismic moment release M_p , there is up to 8 orders of magnitude difference between M_a and M_c which corresponds to just under 5 orders of magnitude difference in terms of moment magnitude M_w . This is intriguing since one the commonest argument to claim that earthquakes do begin as small instabilities that cascade-up grow into larger ruptures ((Beroza & Ellsworth, 1996)) is the lack of detectable seismic activity prior to mainshock. Nucleation process could be so silent that most of the time, the nucleation phase would be difficult to detect.

6 Summary

In this study, we continuously recorded microseismicity generated during stick-slip experiments and analyzed the dynamics of precursory AEs prior to stick-slip instabilities. Using calibrated acoustic sensors we were able to analyze AE source parameters. According to the scaling laws that describe the frequency-magnitude distribution of earthquakes and that link the size of an earthquake to its magnitude, our results suggest that millimetric AEs can be fairly considered as microearthquakes. We found clear evidences that the occurrence of AEs was driven by fault slip acceleration during the nucleation phase of the upcoming stick-slip instability. Precursory AEs share significant similarities with foreshocks at the scale of crustal faults: (i) AE rate increases as an inverse power law of time to failure and (ii) AEs migration, promoted by increasing stress conditions. Having been able to measure the seismic component and the aseismic component of the nucleation phase, we suggested that nucleation is an almost fully aseismic process. This might therefore explain why most of the time, foreshocks are not detected preceding mainshock. Finally, we argued, based on fault surface analysis, that fault strength heterogeneity controls fault coupling. Higher the roughness, stronger the coupling. As a consequence, topographical modifications of the fault during rapid slip episodes such as mechanical abrasion, plastic deformation processes or partial/ complete melting of the fault may reduce or increase fault strength heterogeneity.

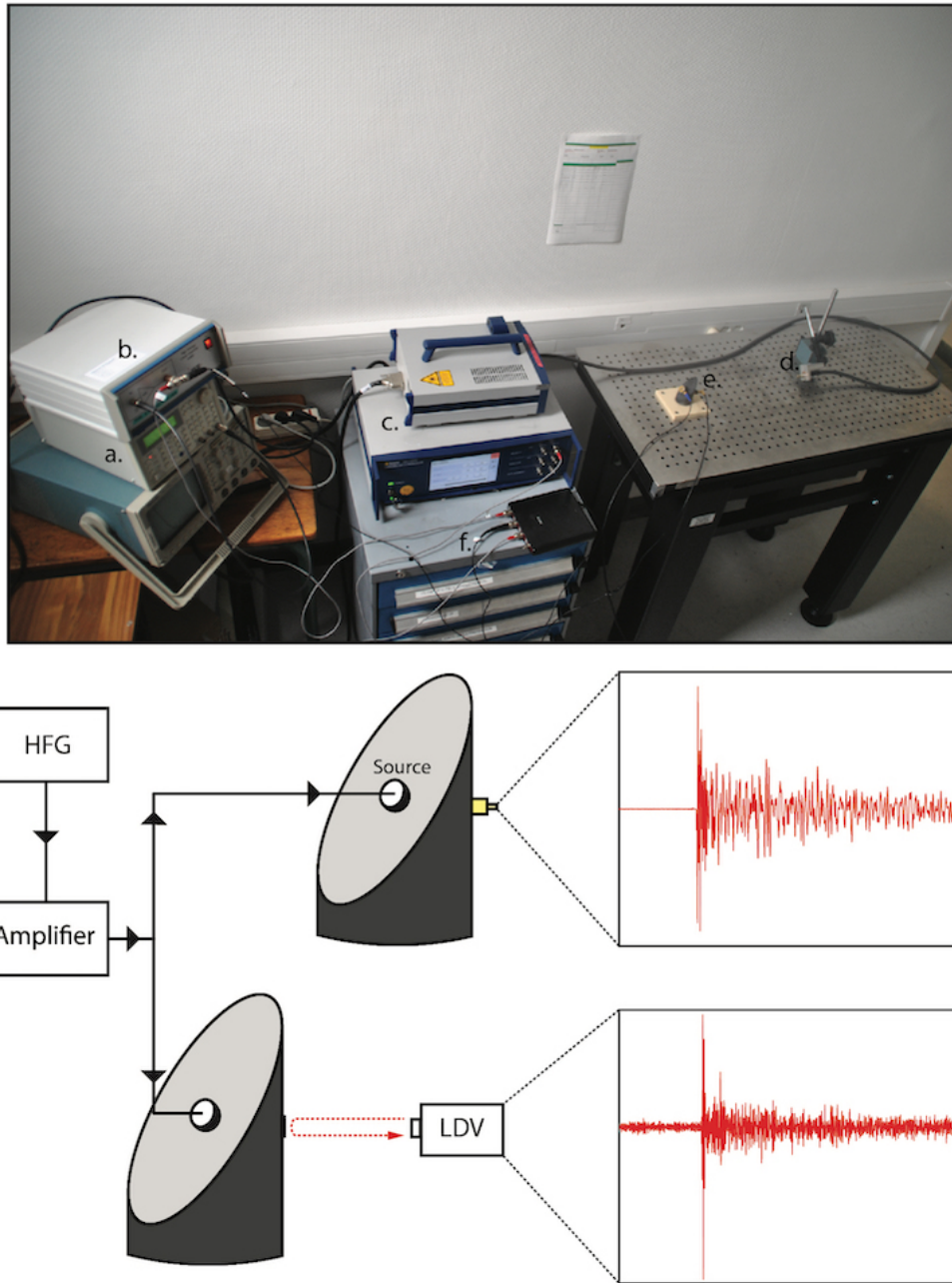


Figure 1. **Top.** Photograph of the experimental set-up used for acoustic sensors calibration. a. High frequency generator (HFG) . b. Amplifier. c. Laser vibrometer acquisition system. d. Laser beam. e. Rock sample with the acoustic sensor and the source glued on. f. Digital oscilloscope. **Bottom.** Schematic view of the calibration procedure. The source is positioned at the center of the fault and subject to an input voltage. Surface vibrations of the opposing side are recorded by the acoustic sensor first and then by LDV.

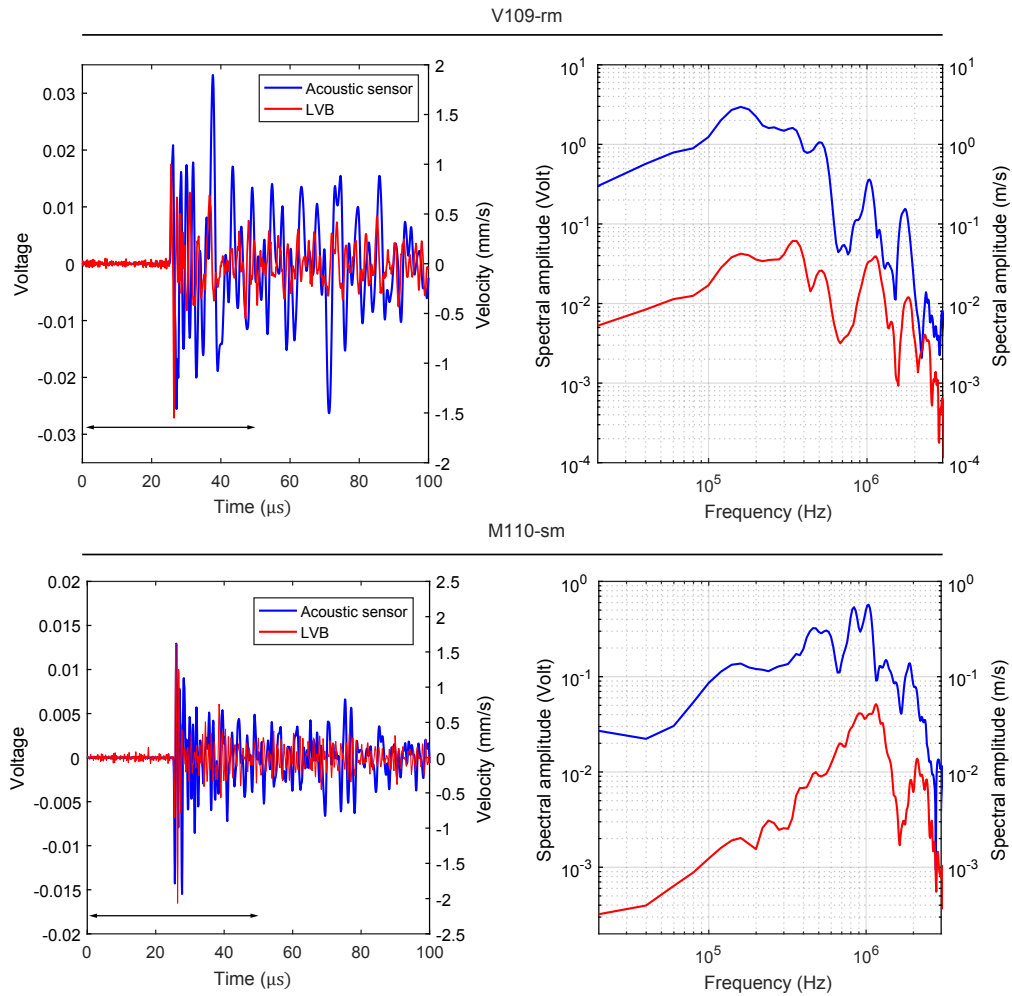


Figure 2. Example of voltage and velocity measurements for the two types of sources and the estimated spectra. The time window used to estimate the spectra is indicated by the black double arrow. This time window is $50 \mu\text{s}$ long and is centered to the first P-wave arrival.

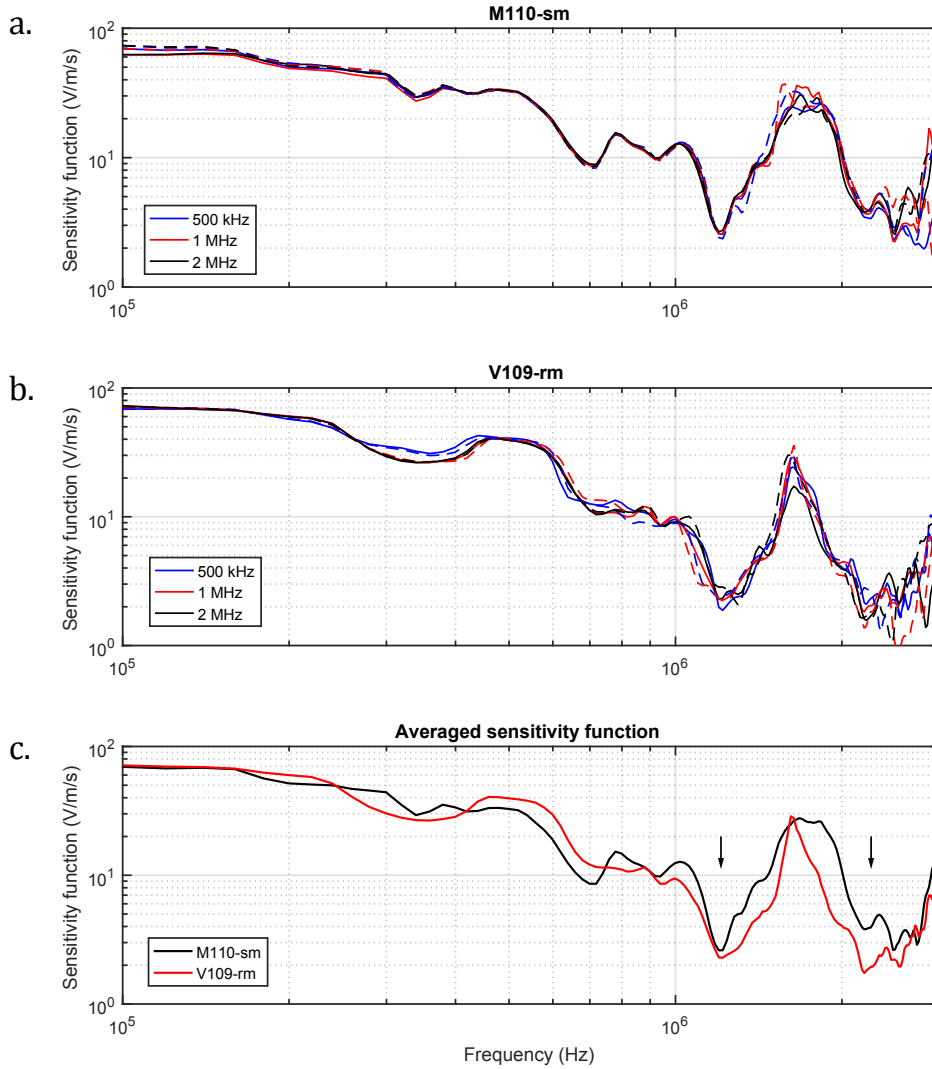


Figure 3. Calibration curves. **a.** Sensitivity functions corresponding to the source M110-sm. The dashed lines indicate the calibration curves obtained for an input voltage of 40 V and the solid lines for an input voltage of 200 V. **b.** Same as **a.** but for the source V109-rm. **c.** Comparison of the sensitivity function averaged over all input voltages and source durations. Acoustic sensors have a net non linear instrumental response showing a large resonance band between 1.2 MHz and 2.2 MHz (delimited by the two black arrows)

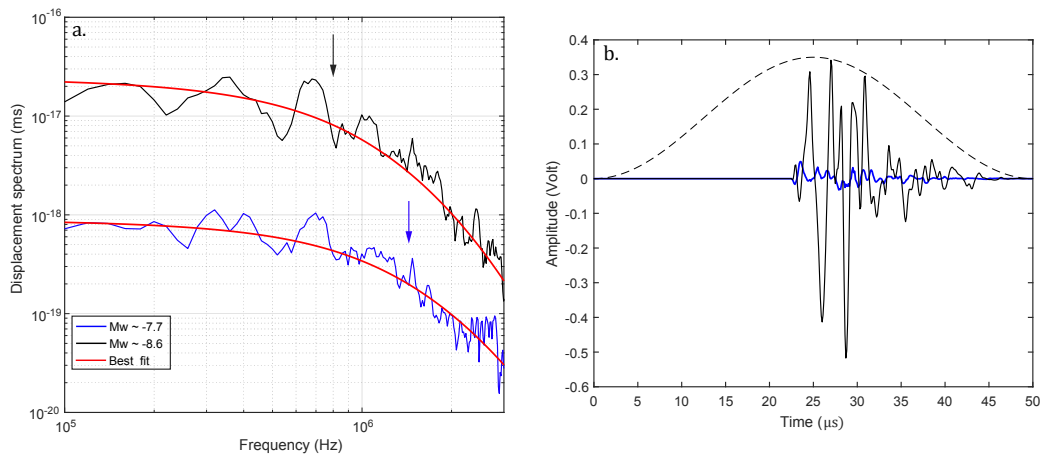


Figure 4. Fitted displacement spectra and acoustic waveforms. **a.** Displacement spectra and best fit for $M_w = 7.7$ and $M_w = 8.6$ events with their respective estimated corner frequencies indicated by the arrows (0.88 MHz and 1.5 MHz , respectively). **b.** Corresponding waveforms used to estimate the spectra, the color code is the same than in **a.** Waveform amplitudes were multiplied by a factor two for visualization. The black dashed line indicates the hanning window used to taper the waveforms.

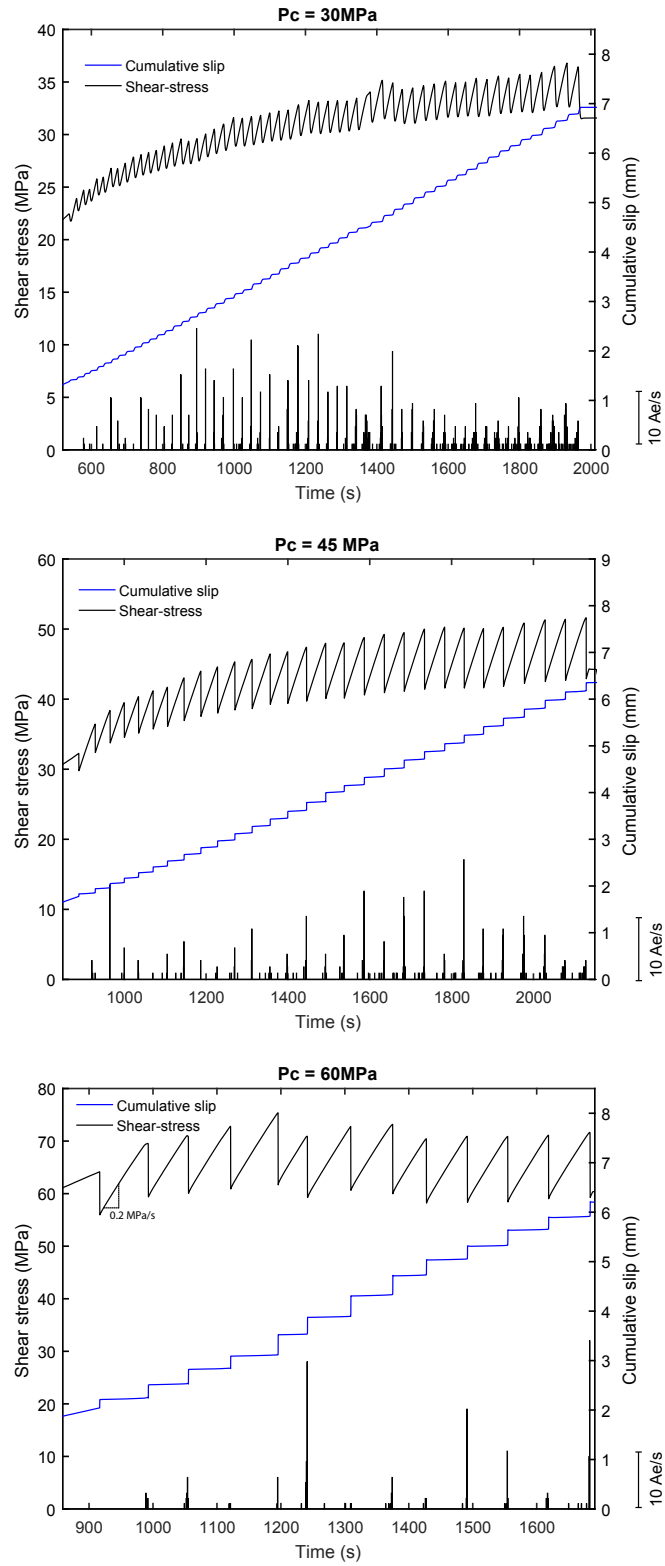


Figure 5. Cumulative slip, shear-stress and AE rate during the experiments. AEs were stacked into 1 second bins. The displacement was corrected from the elastic deformation of the sample and of the apparatus.

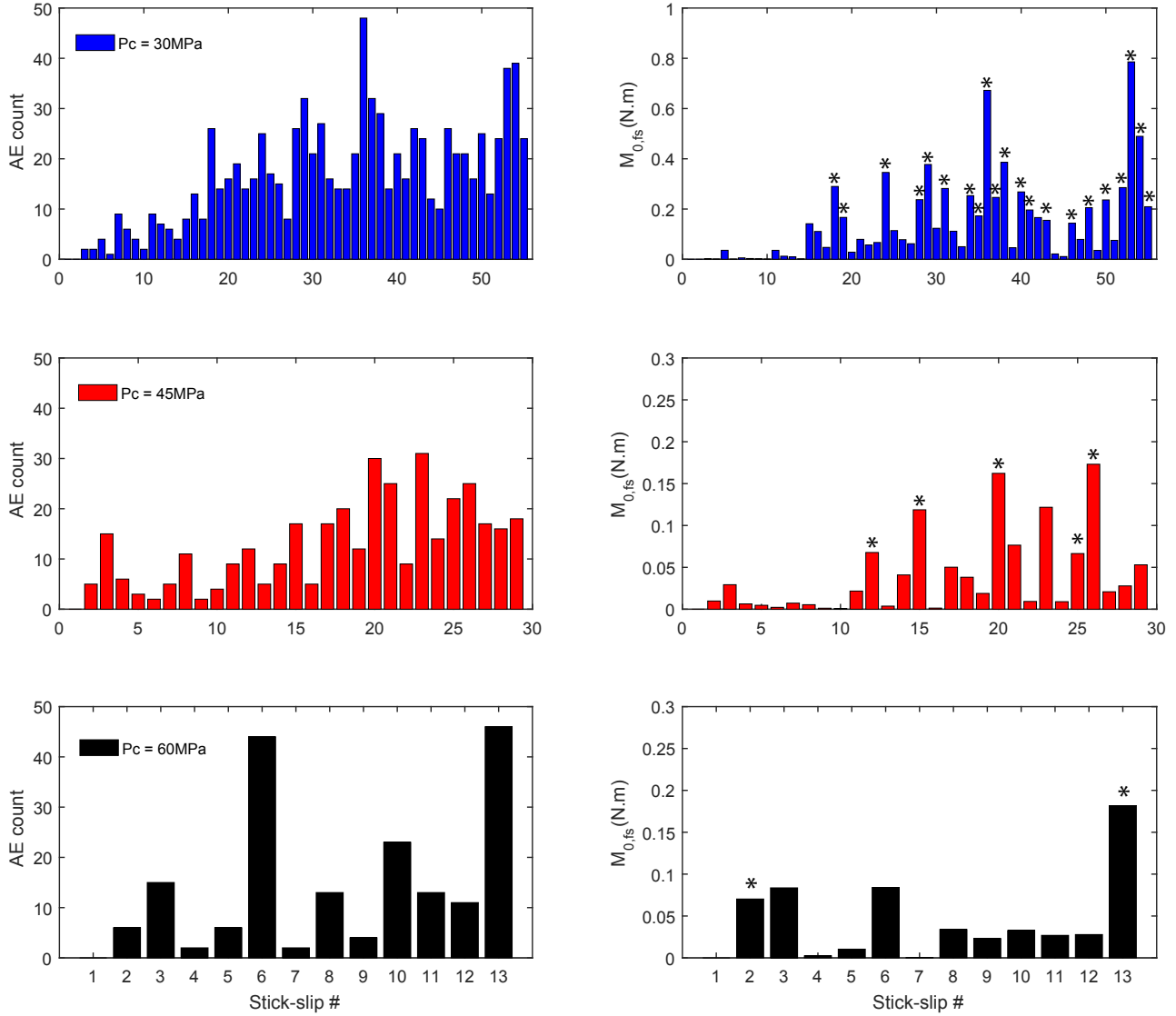


Figure 6. Distribution of the number of AEs (left) and the total AE moment release (right) per stick-slip cycle during the experiments. For particular SSEs, the total AE moment release is a lower bound due to the saturation of the acoustic sensors for $Mw > -7$. Star symbols indicate the AE sequences that contain at least more than 1 AE of $Mw > -7$

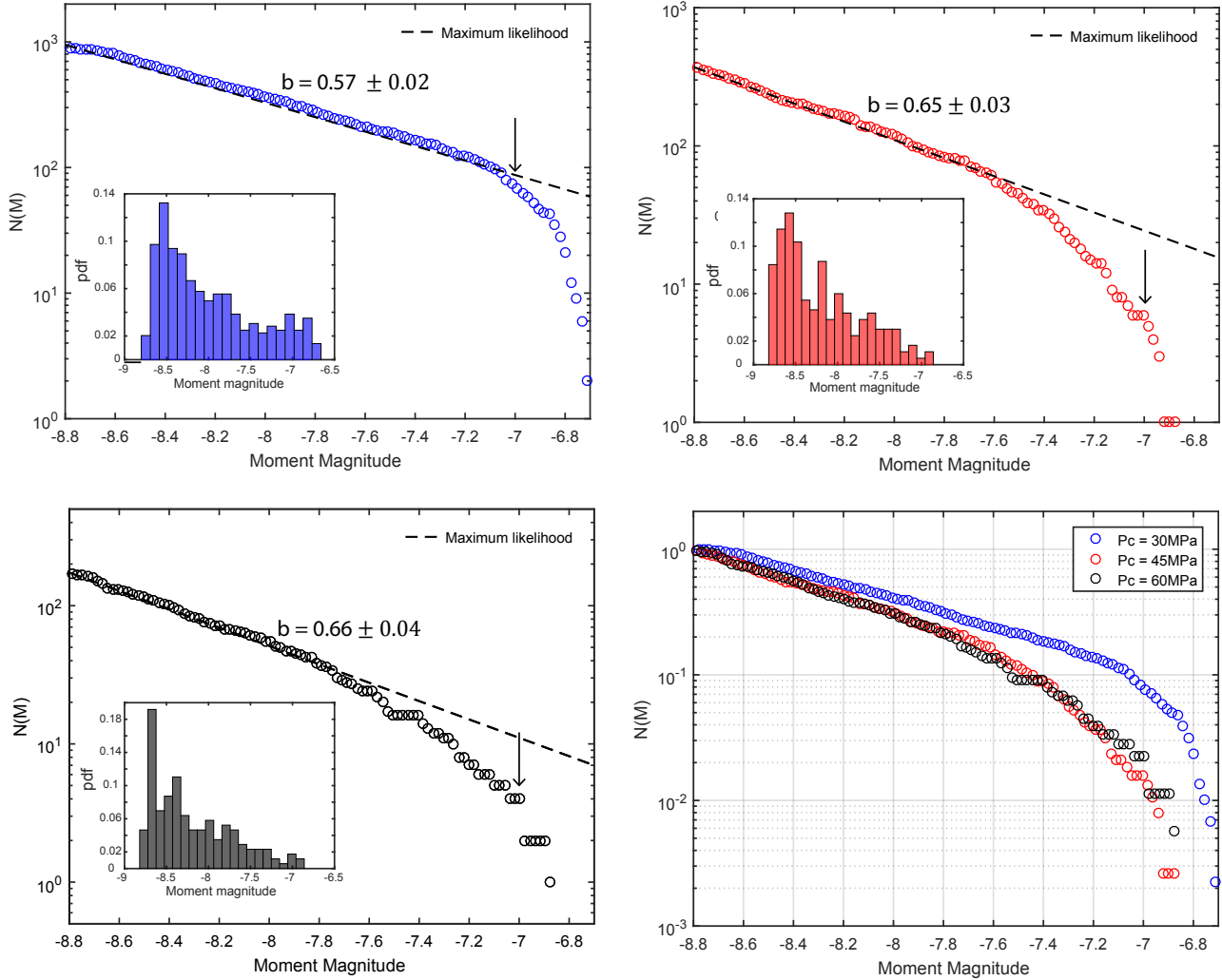


Figure 7. Frequency-magnitude distribution of the generated AEs during the experiments. Colored circles correspond to the cumulative G-R distribution of the AEs moment magnitudes. Black arrows indicate the moment magnitude M_w that correspond to the beginning of the acoustic sensors saturation ($M_w = -7$). Black dashed lines show the b-values that we estimated according to the Aki-Utsu maximum likelihood method. Bar plots are showing the distribution of the AEs moment magnitudes into 0.1 magnitude interval bins.

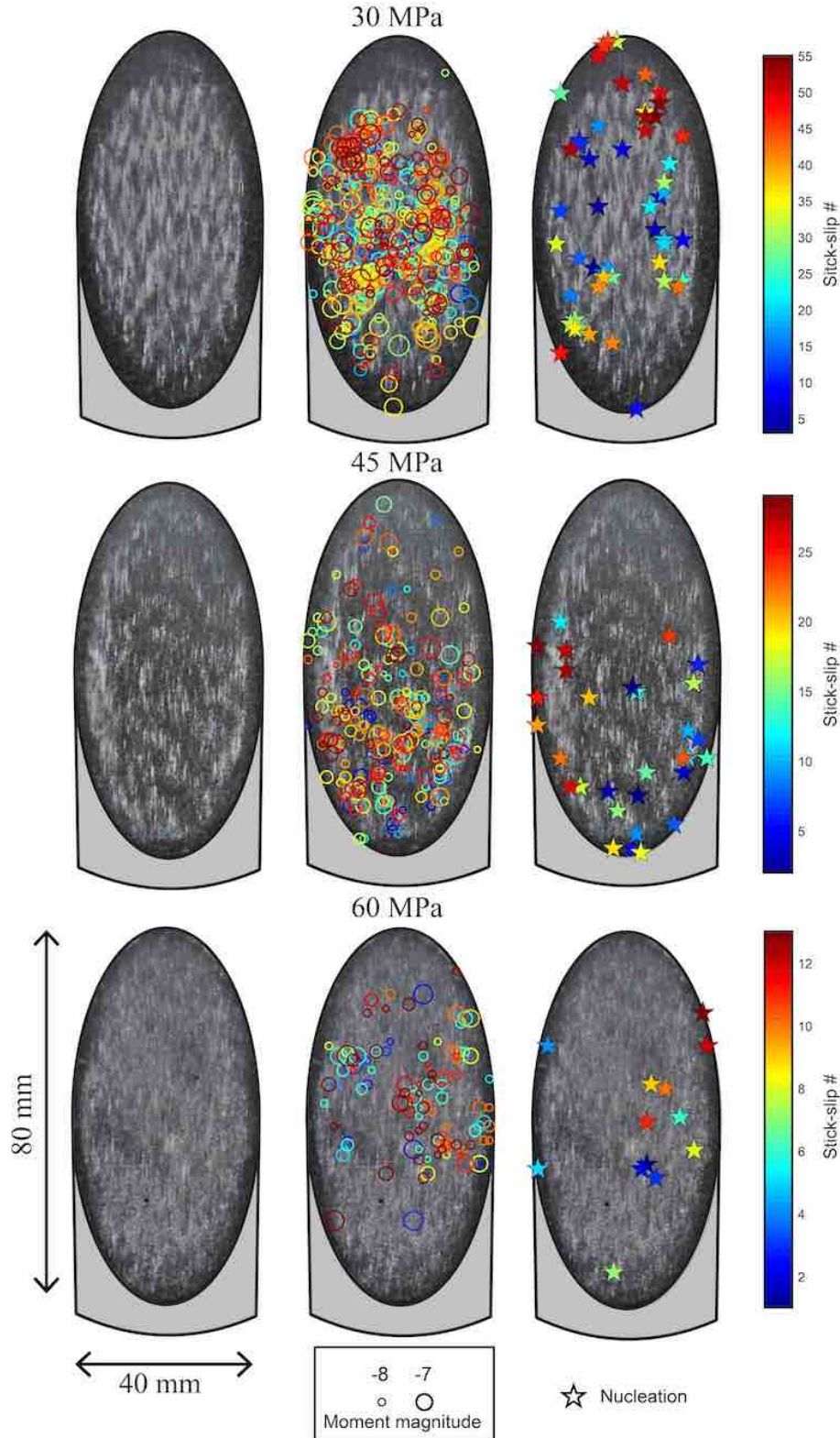


Figure 8. Fault surfaces conditions, AE and stick-slip nucleation locations. Circle size refers to the AE moment magnitude and was set according to the estimated source size. The colorscale refers to the SSE index. Only the AEs whose location errors are less than 2-3 mm are reported here.

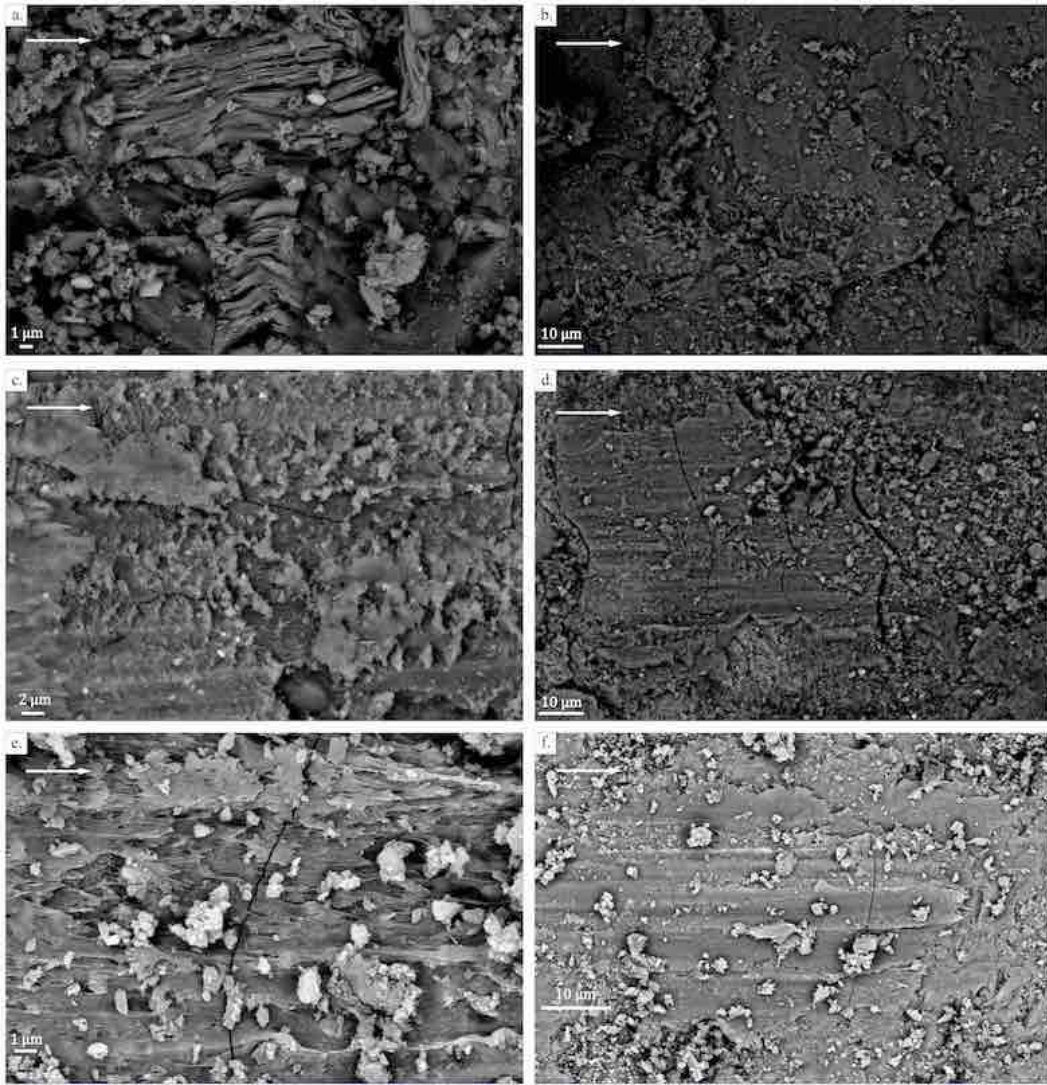


Figure 9. Microtexture of the fault surfaces after stick-slip experiments under Scanning Electron Microscopy at : **a.,b.** $P_c = 30 \text{ MPa}$, **c.,d.** $P_c = 45 \text{ MPa}$ and **e.,f.** $P_c = 60 \text{ MPa}$. The direction of sliding is indicated by the white arrow. **a.** Small scale view of gouge particles with various sizes ranging from few μm to 100 nm . **b.** Large scale view of **a.** showing a highly damaged surface covered with patches of gouge particles heterogeneously distributed. We sense a small scale asperity at the center slightly deformed into the direction of sliding. **c.** Small scale view of amorphous fine gouge particles layer. **d.** Large scale view of **c.** showing clusters of smashed gouge particles with sizes up to $10 \mu\text{s}$. The fault surface presents striations along the sliding direction which suggest plastic deformation during stick-slip events. **e.** Small scale view of the fault surface showing evidence of partial melting during sliding. A fraction of the small gouge particles is trapped into the melt. **f.** Large scale view of **e.** showing stretched and elongated surfaces formed due to partial melting and covered with (more) homogeneously distributed gouge particles.

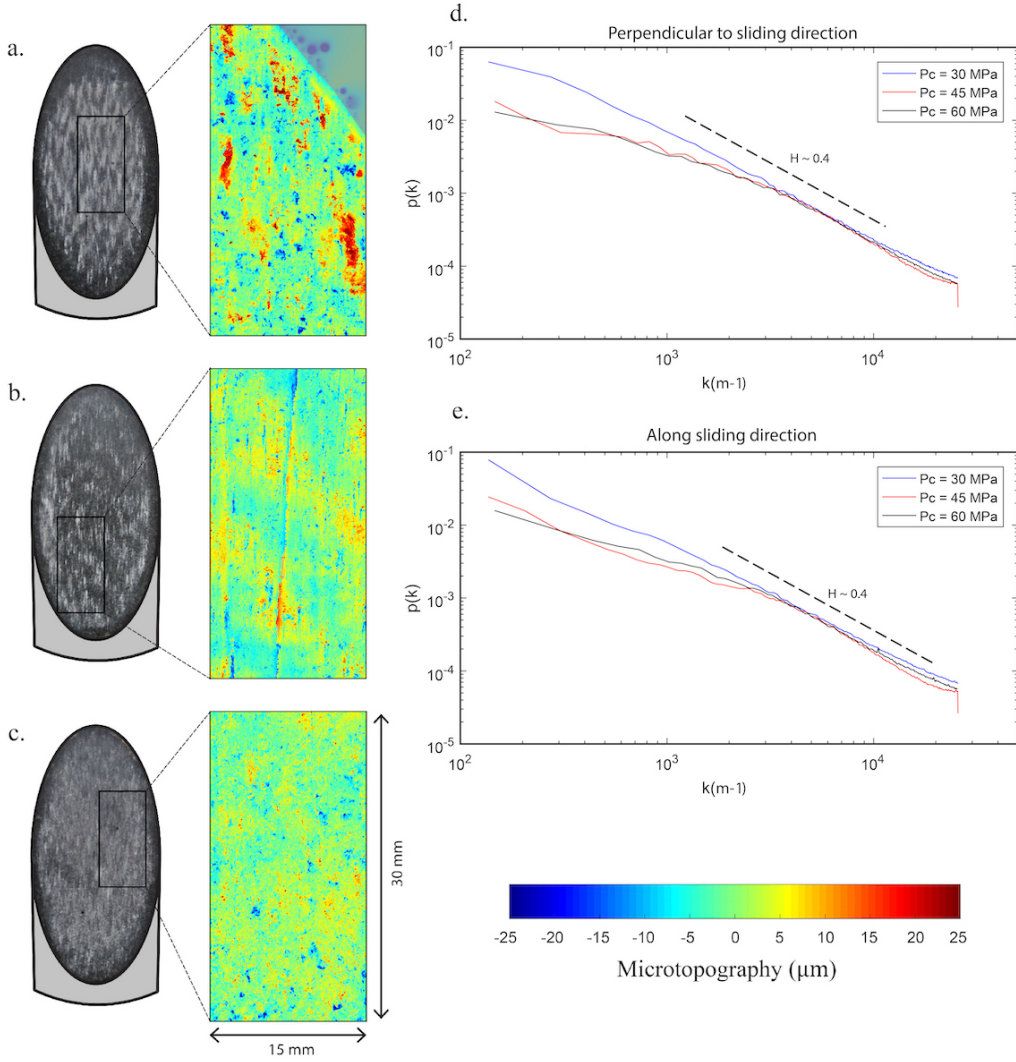


Figure 10. Microtopography of fault surfaces at: a. $P_c = 30$ MPa, b. $P_c = 45$ MPa and c. $P_c = 60$ MPa. The microtopography was measured using a laser profilometer presenting a resolution of $0.05 \mu\text{m}$. The colorscale indicate the microtopography and is given in μm . Sampled surfaces are 15 mm wide and 30 mm long and correspond to the black rectangles shown on the right. **Power spectrum of the fault surfaces microtopography** as a function of the wavenumber k and extracted from the stacking of the 1-D profiles along the perpendicular, **d.** and the parallel directions, **e.**, of the direction of sliding. Black dashed lines represent the power-law expected for a self-affine surface characterized by a Hurst exponent H of 0.4

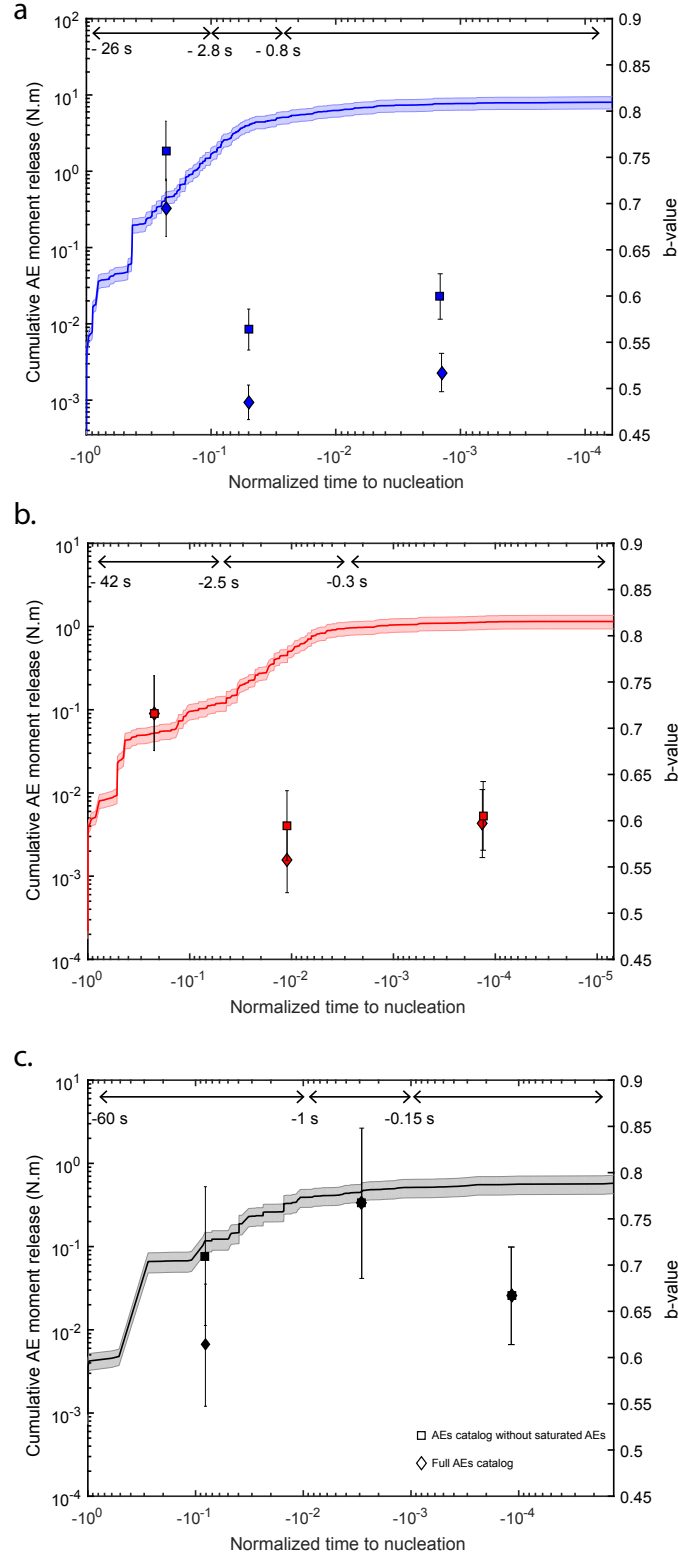


Figure 11. Cumulative AE moment release and b-value evolution prior to failure at : **a.** $P_c = 30$ MPa, **b.** $P_c = 45$ MPa and **c.** $P_c = 60$ MPa. The cumulative AE moment release is relative to the normalized time to failure and results from the stacking of all the precursory AE sequences. Square and diamond symbols show the AEs b-values and their uncertainties that were estimated at various time intervals relative to the onset of stick-slip instability. Square symbols correspond to the b-values that were estimated after removing the saturated AEs ($M_w > 7$) and the diamond symbols show the b-values that were estimated using the full AEs catalogs.

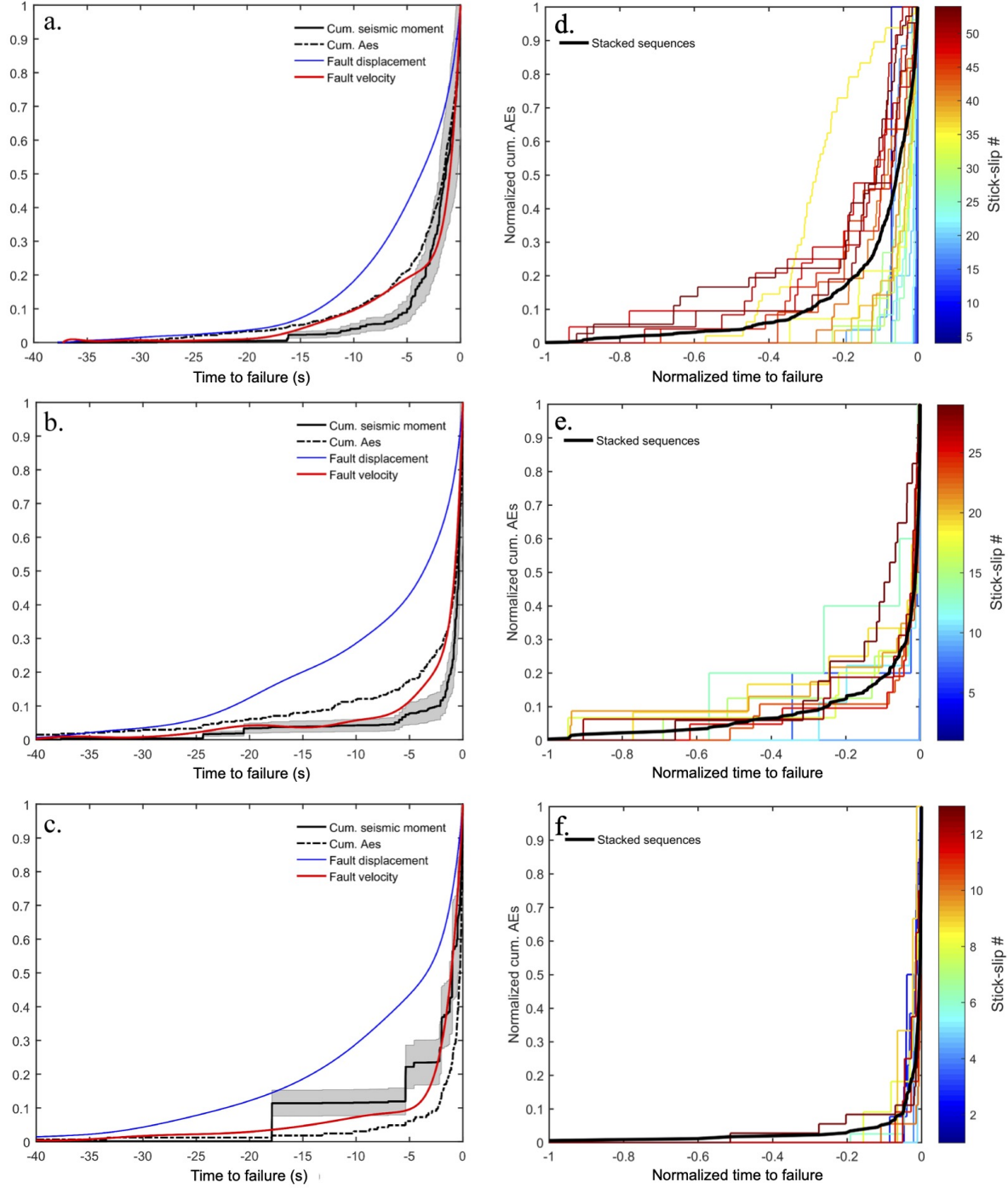


Figure 12. Comparison between the normalized along fault displacement, along fault velocity, cumulative number of AEs and cumulative AE moment release as a function of the normalized time to failure at: a., $P_c = 30$ MPa, b., $P_c = 45$ MPa and c., $P_c = 60$ MPa. All curves result from the stacking of all the SSEs. The grey shaded area around the AE moment release corresponds to the cumulative error of the magnitude estimates. **Evolution of of the normalized cumulative number of AEs as a function of the normalized time to failure at: d., $P_c = 30$ MPa, e., $P_c = 45$ MPa and f., $P_c = 60$ MPa.** The colorscale indicates the SSE index and the black curves result from the stacking of all precursory AE sequences.

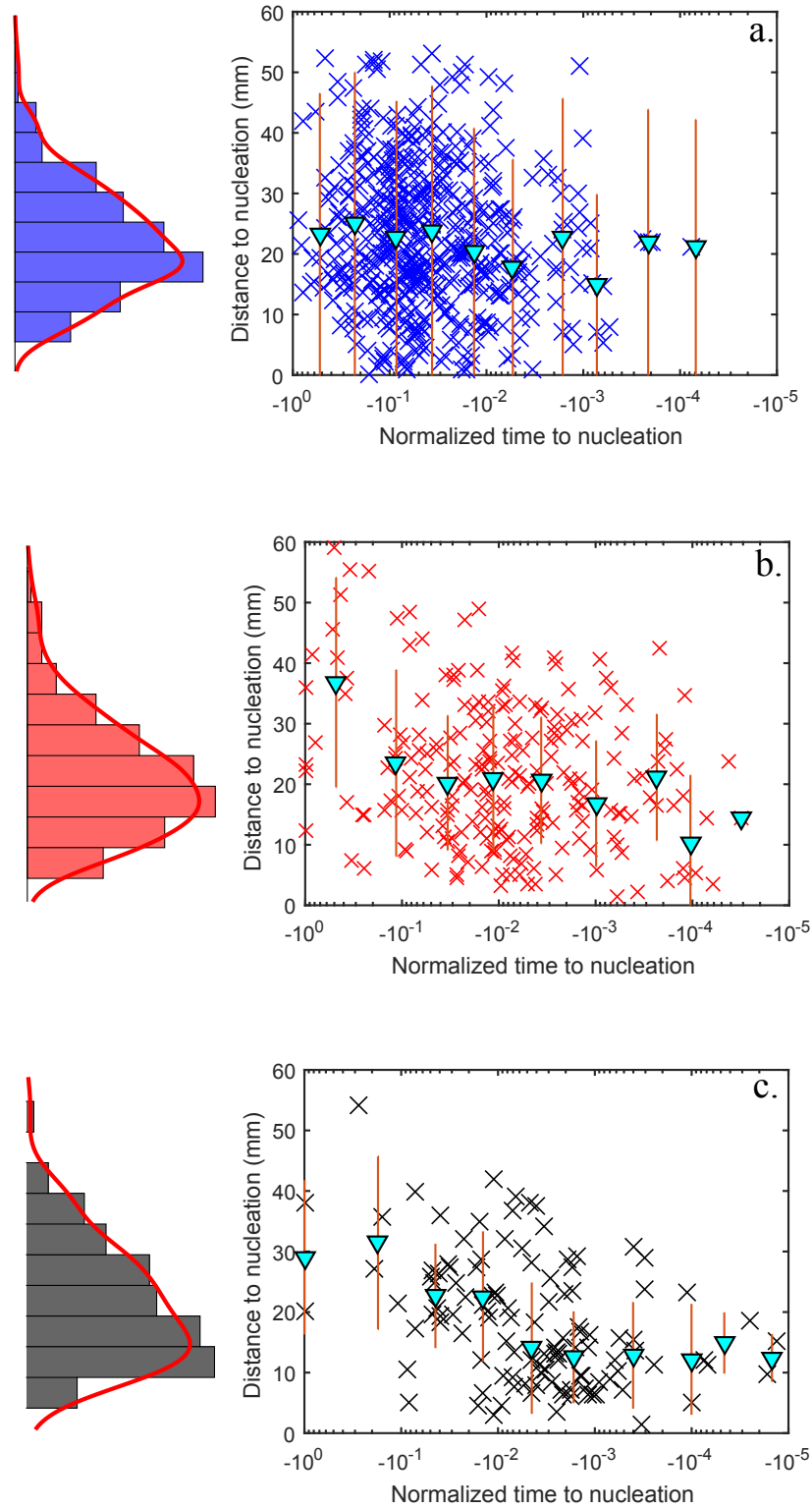


Figure 13. Distance to nucleation of the precursory AEs as a function of the normalized time to failure at : **a.** $P_c = 30$ MPa, **b.** $P_c = 45$ MPa, **c.** $P_c = 45$ MPa. The cyan triangles indicate the average distance to nucleation and its standard deviation computed into 10 log-distributed time intervals. On the left is shown the pdf of the precursory AEs as a function of their distance to nucleation.

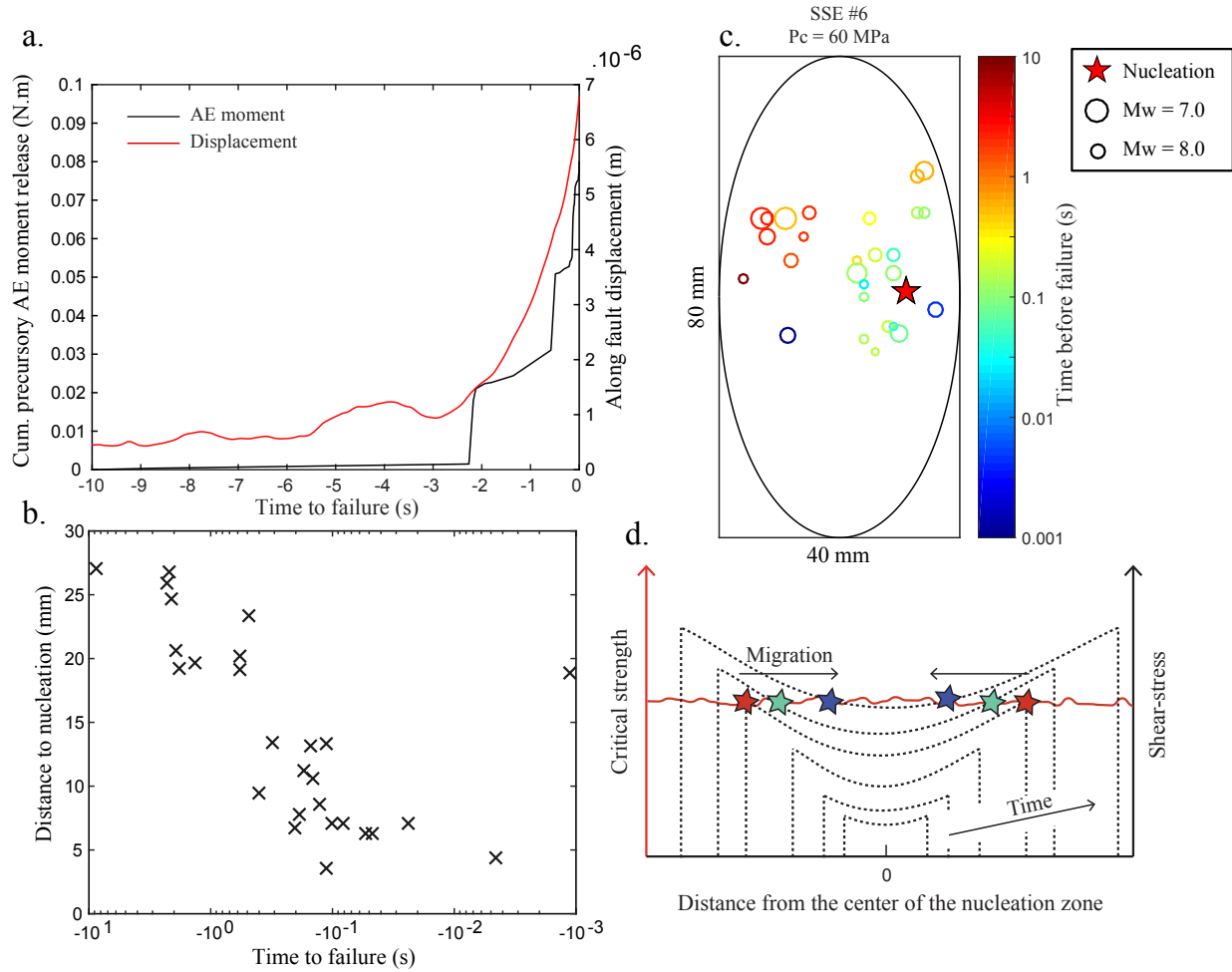


Figure 14. **a.** Cumulative AE moment release and along fault displacement in the last 10 seconds prior to SSE #6 during the experiment conducted at $P_c = 60$ MPa. **b.** Distance to nucleation of the precursory AEs prior to failure. **c.** Locations, sizes and timing of the precursory AEs that occur prior to SSE #6 ($P_c = 60$ MPa). The colorscale refers to the timing of the AEs relative to failure. Circle size indicates the moment magnitude and was set according to source size. The star symbol indicates the nucleation location. **d.** Schematic view of the shear-stress evolution on locked portions of the fault (i.e., in the interior of the nucleation zone) during nucleation. The black dashed lines indicate the shear-stress profile. The red line idealizes the critical strength of the locked fault patches in the case of an homogeneous medium. The star symbols depict the schematic view of the migration in time and space of the precursory AEs towards nucleation initiation. The stress perturbations at the tips of the nucleation zone trigger the precursory AE activity far from nucleation. As the nucleation zone expands, stresses build-up in the interior of the nucleation. The shear-stress gradient leads to the migration of the precursory AEs towards the center of the nucleation zone.

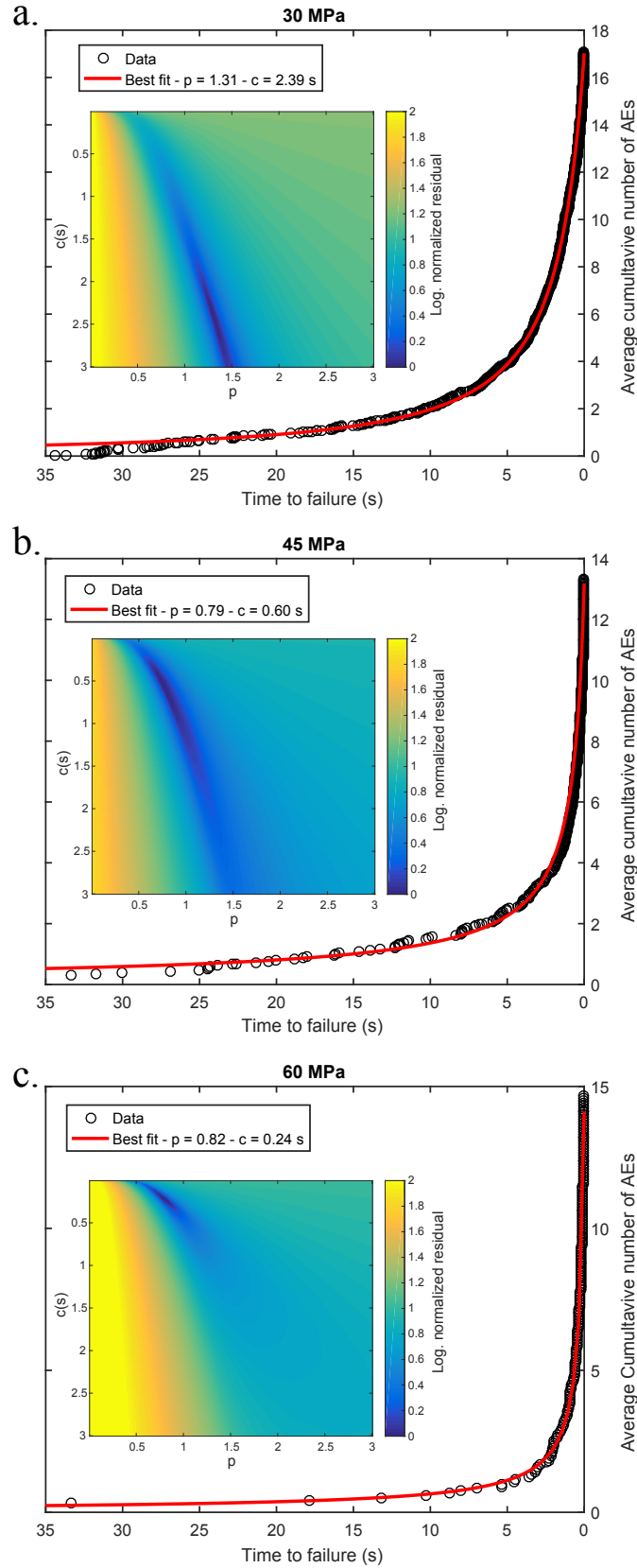


Figure 15. Inverse power law of time of the average cumulative number of AEs towards failure at: **a.** $P_c = 30$ MPa, **b.** $P_c = 45$ MPa and **c.** $P_c = 60$ MPa. The red curves indicate the best fits obtained on parameters c and p . The inserted figures display the logarithm of the residuals normalized by the minimum (i.e., 0 indicates the minimum) as a function of c and p

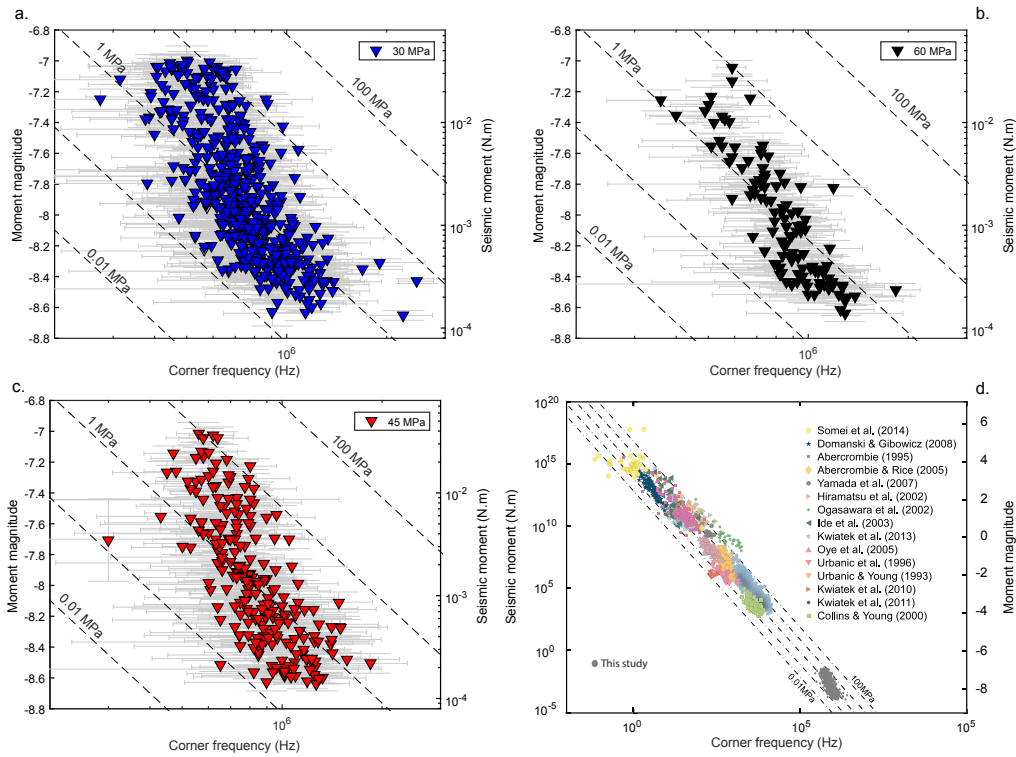


Figure 16. Relationship between M_0 and f_c at: **a.** $P_c = 30$ MPa, **b.** $P_c = 45$ MPa and **c.** $P_c = 60$ MPa. Dashed black lines represent stress drops of 0.01, 0.1, 1, 10, 100 MPa from Madariaga’s source model (Madariaga, 1976). **d.** The AEs source parameters for all the experiments are plotted as gray circles. The other points represent a corpus of previous studies and were taken from (Yoshimitsu et al., 2014).

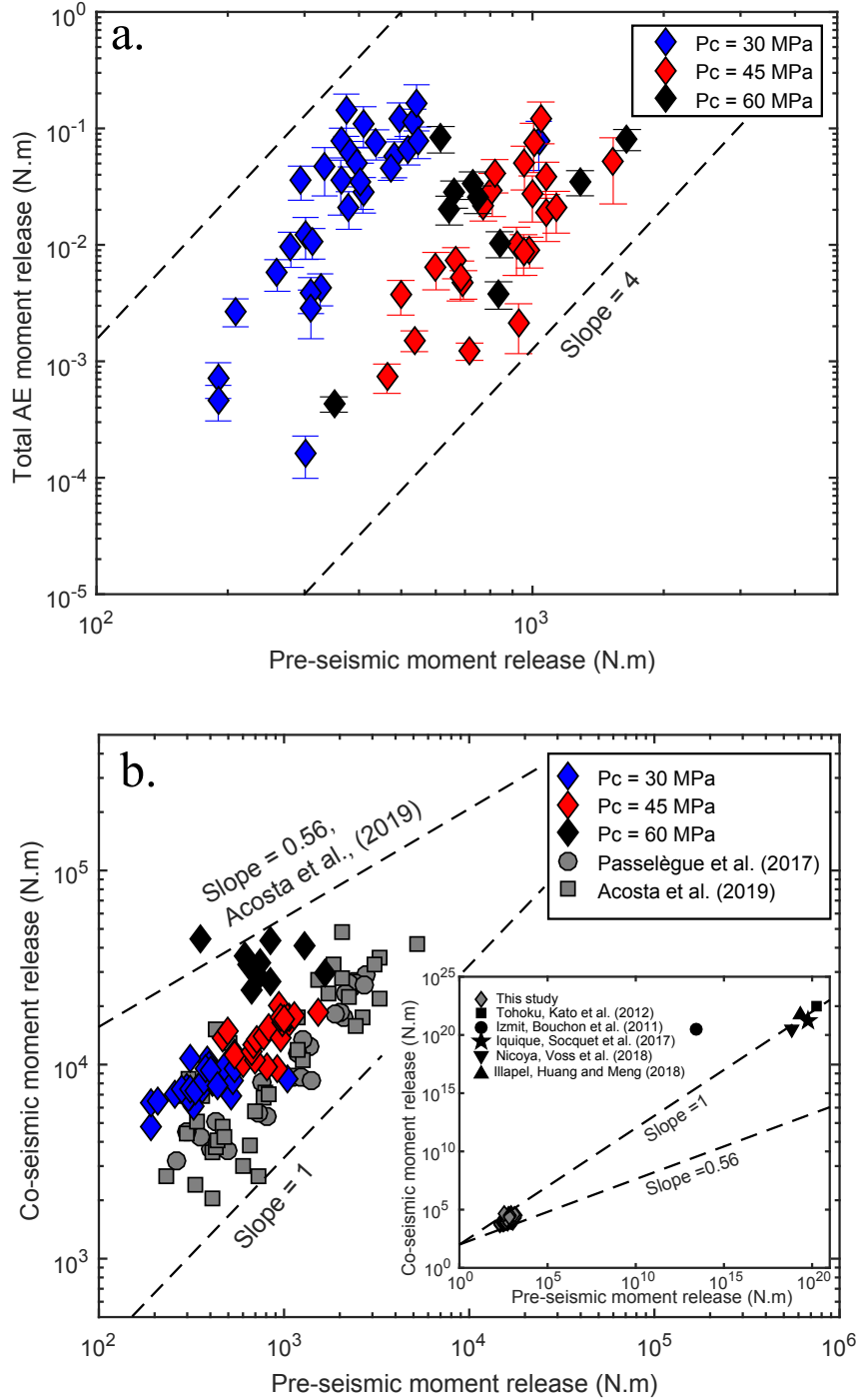


Figure 17. **a.** Relationship between the pre-seismic moment release and the total AE moment release. Each diamond represents one SSE. Only the AE sequences that do not contain saturated AEs are shown here. The black-dashed lines indicates a power-law exponents of 4. **b.** Relationship between the pre-seismic moment release and the co-seismic moment release. The grey squares and circles correspond to the observations of two other experimental studies (Passelègue et al., 2017; Acosta et al., 2019). The black dashed line which indicates a slope of 0.56 corresponds to the scaling law between the pre-seismic moment release M_p and the co-seismic moment release M_c proposed by Acosta et al. (2019). A linear relation between both is given by the black dashed line whose slope = 1. The inserted figure displays the comparison between our observations and what was found for a set of large earthquakes ($M_w \geq 7.6$).

Acknowledgments

This work was funded by the European Research Council grant REALISM (2016-grant 681346). The authors declare that they have no competing financial interests. H.S.B. would like to acknowledge funding from the European Research Council grant PER-SISMO (865411). All data are available online (<https://github.com/samsonmarty/high-frequency-radiation-during-laboratory-earthquakes>).

References

- Abercrombie, R. E. (1995). Earthquake source scaling relationships from- 1 to 5 ml using seismograms recorded at 2.5-km depth. *Journal of Geophysical Research: Solid Earth*, *100*(B12), 24015–24036.
- Abercrombie, R. E., & Mori, J. (1996). Occurrence patterns of foreshocks to large earthquakes in the western united states. *Nature*, *381*(6580), 303.
- Abercrombie, R. E., & Rice, J. R. (2005). Can observations of earthquake scaling constrain slip weakening? *Geophysical Journal International*, *162*(2), 406–424.
- Acosta, M., Passelègue, F. X., Schubnel, A., Madariaga, R., & Violay, M. (2019). Precursory moment release scales with earthquake magnitude. *arXiv preprint arXiv:1901.06908*.
- Aki, K. (1967). Scaling law of seismic spectrum. *Journal of geophysical research*, *72*(4), 1217–1231.
- Aki, K., & Richards, P. G. (2002). *Quantitative seismology*.
- Ampuero, J.-P., & Rubin, A. M. (2008). Earthquake nucleation on rate and state faults—aging and slip laws. *Journal of Geophysical Research: Solid Earth*, *113*(B1).
- Beroza, G. C., & Ellsworth, W. L. (1996). Properties of the seismic nucleation phase. *Tectonophysics*, *261*(1-3), 209–227.
- Bouchon, M., Durand, V., Marsan, D., Karabulut, H., & Schmittbuhl, J. (2013). The long precursory phase of most large interplate earthquakes. *Nature geoscience*, *6*(4), 299.
- Bouchon, M., Karabulut, H., Aktar, M., Özalaybey, S., Schmittbuhl, J., & Bouin, M.-P. (2011). Extended nucleation of the 1999 mw 7.6 izmit earthquake. *science*, *331*(6019), 877–880.
- Campillo, M., & Ionescu, I. R. (1997). Initiation of antiplane shear instability under slip dependent friction. *Journal of Geophysical Research: Solid Earth*, *102*(B9), 20363–20371.
- Candela, T., Renard, F., Bouchon, M., Brouste, A., Marsan, D., Schmittbuhl, J., & Voisin, C. (2009). Characterization of fault roughness at various scales: Implications of three-dimensional high resolution topography measurements. In *Mechanics, structure and evolution of fault zones* (pp. 1817–1851). Springer.
- Cocco, M., Tinti, E., Marone, C., & Piatanesi, A. (2009). Scaling of slip weakening distance with final slip during dynamic earthquake rupture. *International Geophysics*, *94*, 163–186.
- Dieterich, J. (1994). A constitutive law for rate of earthquake production and its application to earthquake clustering. *Journal of Geophysical Research: Solid Earth*, *99*(B2), 2601–2618.
- Ellsworth, W., & Beroza, G. (1995). Seismic evidence for an earthquake nucleation phase. *Science*, *268*(5212), 851–855.
- Enescu, B., & Ito, K. (2001). Some premonitory phenomena of the 1995 hyogo-ken nanbu (kobe) earthquake: seismicity, b-value and fractal dimension. *Tectonophysics*, *338*(3-4), 297–314.
- Eshelby, J. D. (1957). The determination of the elastic field of an ellipsoidal inclusion, and related problems. *Proceedings of the Royal Society of London. Series A. Mathematical and Physical Sciences*, *241*(1226), 376–396.

- Fang, Z., Dieterich, J. H., & Xu, G. (2010). Effect of initial conditions and loading path on earthquake nucleation. *Journal of Geophysical Research: Solid Earth*, *115*(B6).
- Fukuyama, E., Tsuchida, K., Kawakata, H., Yamashita, F., Mizoguchi, K., & Xu, S. (2018). Spatiotemporal complexity of 2-d rupture nucleation process observed by direct monitoring during large-scale biaxial rock friction experiments. *Tectonophysics*, *733*, 182–192.
- Goebel, T., Becker, T., Schorlemmer, D., Stanchits, S., Sammis, C., Rybacki, E., & Dresen, G. (2012). Identifying fault heterogeneity through mapping spatial anomalies in acoustic emission statistics. *Journal of Geophysical Research: Solid Earth*, *117*(B3).
- Goldberg, D., Badri, M., & Wepfer, W. (1992). Acoustic attenuation in oceanic gabbro. *Geophysical Journal International*, *111*(2), 193–202.
- Hartley, R., & Behringer, R. (2003). Logarithmic rate dependence of force networks in sheared granular materials. *Nature*, *421*(6926), 928.
- Helmstetter, A., & Sornette, D. (2003b). Foreshocks explained by cascades of triggered seismicity. *Journal of Geophysical Research: Solid Earth*, *108*(B10).
- Hiramatsu, Y., Yamanaka, H., Tadokoro, K., Nishigami, K. y., & Ohmi, S. (2002). Scaling law between corner frequency and seismic moment of microearthquakes: Is the breakdown of the cube law a nature of earthquakes? *Geophysical research letters*, *29*(8), 52–1.
- Huang, H., & Meng, L. (2018). Slow unlocking processes preceding the 2015 mw 8.4 Illapel, Chile, earthquake. *Geophysical Research Letters*, *45*(9), 3914–3922.
- Ida, Y. (1972). Cohesive force across the tip of a longitudinal-shear crack and Griffith's specific surface energy. *Journal of Geophysical Research*, *77*(20), 3796–3805.
- Ide, S., & Takeo, M. (1997). Determination of constitutive relations of fault slip based on seismic wave analysis. *Journal of Geophysical Research: Solid Earth*, *102*(B12), 27379–27391.
- Jones, L., & Molnar, P. (1976). Frequency of foreshocks. *Nature*, *262*(5570), 677.
- Jones, L. M., & Molnar, P. (1979). Some characteristics of foreshocks and their possible relationship to earthquake prediction and premonitory slip on faults. *Journal of Geophysical Research: Solid Earth*, *84*(B7), 3596–3608.
- Kaneko, Y., & Lapusta, N. (2008). Variability of earthquake nucleation in continuum models of rate-and-state faults and implications for aftershock rates. *Journal of Geophysical Research: Solid Earth*, *113*(B12).
- Kato, A., Fukuda, J., Kumazawa, T., & Nakagawa, S. (2016). Accelerated nucleation of the 2014 Iquique, Chile mw 8.2 earthquake. *Scientific reports*, *6*, 24792.
- Kato, A., & Nakagawa, S. (2014). Multiple slow-slip events during a foreshock sequence of the 2014 Iquique, Chile mw 8.1 earthquake. *Geophysical Research Letters*, *41*(15), 5420–5427.
- Kato, A., Obara, K., Igarashi, T., Tsuruoka, H., Nakagawa, S., & N. (2012). Propagation of slow slip leading up to the 2011 mw 9.0 Tohoku-oki earthquake. *Science*, *335*(6069), 705–708.
- Kwiatek, G., Goebel, T., & Dresen, G. (2014). Seismic moment tensor and b value variations over successive seismic cycles in laboratory stick-slip experiments. *Geophysical Research Letters*, *41*(16), 5838–5846.
- Kwiatek, G., Plenkers, K., Dresen, G., & Group, J. R. (2011). Source parameters of picoseismicity recorded at Mponeng deep gold mine, South Africa: Implications for scaling relations. *Bulletin of the Seismological Society of America*, *101*(6), 2592–2608.
- Lapusta, N., & Rice, J. R. (2003). Nucleation and early seismic propagation of small and large events in a crustal earthquake model. *Journal of Geophysical Research: Solid Earth*, *108*(B4).
- Latour, S., Schubnel, A., Nielsen, S., Madariaga, R., & Vinciguerra, S. (2013). Char-

- acterization of nucleation during laboratory earthquakes. *Geophysical Research Letters*, *40*(19), 5064–5069.
- Lei, X., Li, S., & Liu, L. (2018). Seismic b-value for foreshock ae events preceding repeated stick-slips of pre-cut faults in granite. *Applied Sciences*, *8*(12), 2361.
- Liu, C., & Ahrens, T. J. (1997). Stress wave attenuation in shock-damaged rock. *Journal of Geophysical Research: Solid Earth*, *102*(B3), 5243–5250.
- Madariaga, R. (1976). Dynamics of an expanding circular fault. *Bulletin of the Seismological Society of America*, *66*(3), 639–666.
- Mair, K., Frye, K. M., & Marone, C. (2002). Influence of grain characteristics on the friction of granular shear zones. *Journal of Geophysical Research: Solid Earth*, *107*(B10), ECV-4.
- Marone, C. (1998). Laboratory-derived friction laws and their application to seismic faulting. *Annual Review of Earth and Planetary Sciences*, *26*(1), 643–696.
- Marsan, D., Helmstetter, A., Bouchon, M., & Dublanchet, P. (2014). Foreshock activity related to enhanced aftershock production. *Geophysical Research Letters*, *41*(19), 6652–6658.
- McGuire, J. J., Boettcher, M. S., & Jordan, T. H. (2005). Foreshock sequences and short-term earthquake predictability on east pacific rise transform faults. *Nature*, *434*(7032), 457.
- McLaskey, G. C., & Kilgore, B. D. (2013). Foreshocks during the nucleation of stick-slip instability. *Journal of Geophysical Research: Solid Earth*, *118*(6), 2982–2997.
- McLaskey, G. C., & Lockner, D. A. (2014). Preslip and cascade processes initiating laboratory stick slip. *Journal of Geophysical Research: Solid Earth*, *119*(8), 6323–6336.
- McLaskey, G. C., Lockner, D. A., Kilgore, B. D., & Beeler, N. M. (2015). A robust calibration technique for acoustic emission systems based on momentum transfer from a ball drop. *Bulletin of the Seismological Society of America*, *105*(1), 257–271.
- Moreno, M., Li, S., Angiboust, S., Schurr, B., Bedford, J., & Oncken, O. (2015). The 2014 iquique chile earthquake: Preparatory breaking processes of a locked asperity and natural constraints for fluid migration along the plate interface. In *Agu fall meeting abstracts*.
- Nanjo, K., Hirata, N., Obara, K., & Kasahara, K. (2012). Decade-scale decrease in b-value prior to the m9-class 2011 tohoku and 2004 sumatra quakes. *Geophysical Research Letters*, *39*(20).
- Nielsen, S., Taddeucci, J., & Vinciguerra, S. (2010). Experimental observation of stick-slip instability fronts. *Geophysical Journal International*, *180*(2), 697–702.
- Ogata, Y. (1983). Estimation of the parameters in the modified omori formula for aftershock frequencies by the maximum likelihood procedure. *Journal of Physics of the Earth*, *31*(2), 115–124.
- Ogata, Y. (1988). Statistical models for earthquake occurrences and residual analysis for point processes. *Journal of the American Statistical Association*, *83*(401), 9–27.
- Ohnaka, M. (2003). A constitutive scaling law and a unified comprehension for frictional slip failure, shear fracture of intact rock, and earthquake rupture. *Journal of Geophysical Research: Solid Earth*, *108*(B2).
- Ohnaka, M. (2013). *The physics of rock failure and earthquakes*. Cambridge University Press.
- Ohnaka, M., & Kuwahara, Y. (1990). Characteristic features of local breakdown near a crack-tip in the transition zone from nucleation to unstable rupture during stick-slip shear failure. *Tectonophysics*, *175*(1-3), 197–220.
- Ojala, I. O., Main, I. G., & Ngwenya, B. T. (2004). Strain rate and temperature dependence of omori law scaling constants of ae data: Implications for earth-

- quake foreshock-aftershock sequences. *Geophysical Research Letters*, 31(24).
- Okubo, P. G., & Dieterich, J. H. (1984). Effects of physical fault properties on frictional instabilities produced on simulated faults. *Journal of Geophysical Research: Solid Earth*, 89(B7), 5817–5827.
- Olsen, K., Madariaga, R., & Archuleta, R. J. (1997). Three-dimensional dynamic simulation of the 1992 landers earthquake. *Science*, 278(5339), 834–838.
- Palmer, A. C., & Rice, J. R. (1973). The growth of slip surfaces in the progressive failure of over-consolidated clay. *Proceedings of the Royal Society of London. A. Mathematical and Physical Sciences*, 332(1591), 527–548.
- Papazachos, B. C. (1973). The time distribution of the reservoir-associated foreshocks and its importance to the prediction of the principal shock. *Bulletin of the Seismological Society of America*, 63(6-1), 1973–1978.
- Passelègue, F. X., Latour, S., Schubnel, A., Nielsen, S., Bhat, H. S., & Madariaga, R. (2017). Influence of fault strength on precursory processes during laboratory earthquakes. *Fault Zone Dynamic Processes: Evolution of Fault Properties During Seismic Rupture*, 227, 229.
- Passelègue, F. X., Schubnel, A., Nielsen, S., Bhat, H. S., Deldicque, D., & Madariaga, R. (2016). Dynamic rupture processes inferred from laboratory microearthquakes. *Journal of Geophysical Research: Solid Earth*, 121(6), 4343–4365.
- Prieto, G. A., Shearer, P. M., Vernon, F. L., & Kilb, D. (2004). Earthquake source scaling and self-similarity estimation from stacking p and s spectra. *Journal of Geophysical Research: Solid Earth*, 109(B8).
- Rice, J. (1979). *The mechanics of earthquake rupture*. Division of Engineering, Brown University Providence.
- Rivière, J., Lv, Z., Johnson, P., & Marone, C. (2018). Evolution of b-value during the seismic cycle: Insights from laboratory experiments on simulated faults. *Earth and Planetary Science Letters*, 482, 407–413.
- Rubin, A. M., & Ampuero, J.-P. (2005). Earthquake nucleation on (aging) rate and state faults. *Journal of Geophysical Research: Solid Earth*, 110(B11).
- Ruiz, S., Metois, M., Fuenzalida, A., Ruiz, J., Leyton, F., Grandin, R., . . . Campos, J. (2014). Intense foreshocks and a slow slip event preceded the 2014 iquique mw 8.1 earthquake. *Science*, 345(6201), 1165–1169.
- Schaff, D. P., Bokelmann, G. H., Beroza, G. C., Waldhauser, F., & Ellsworth, W. L. (2002). High-resolution image of calaveras fault seismicity. *Journal of Geophysical Research: Solid Earth*, 107(B9), ESE–5.
- Scholz, C. (1968b). The frequency-magnitude relation of microfracturing in rock and its relation to earthquakes. *Bulletin of the seismological society of America*, 58(1), 399–415.
- Socquet, A., Valdes, J. P., Jara, J., Cotton, F., Walpersdorf, A., Cotte, N., . . . Norabuena, E. (2017). An 8 month slow slip event triggers progressive nucleation of the 2014 chile megathrust. *Geophysical Research Letters*, 44(9), 4046–4053.
- Suyehiro, S. (1966). Difference between aftershocks and foreshocks in the relationship of magnitude to frequency of occurrence for the great chilean earthquake of 1960. *Bulletin of the Seismological Society of America*, 56(1), 185–200.
- Tamaribuchi, K., Yagi, Y., Enescu, B., & Hirano, S. (2018). Characteristics of foreshock activity inferred from the jma earthquake catalog. *Earth, Planets and Space*, 70(1), 90.
- Thompson, B., Young, R., & Lockner, D. A. (2009). Premonitory acoustic emissions and stick-slip in natural and smooth-faulted westerly granite. *Journal of Geophysical Research: Solid Earth*, 114(B2).
- Tormann, T., Enescu, B., Woessner, J., & Wiemer, S. (2015). Randomness of megathrust earthquakes implied by rapid stress recovery after the japan earthquake. *Nature Geoscience*, 8(2), 152.
- Uenishi, K., & Rice, J. R. (2003). Universal nucleation length for slip-weakening

- rupture instability under nonuniform fault loading. *Journal of Geophysical Research: Solid Earth*, 108(B1).
- Voss, N., Dixon, T. H., Liu, Z., Malservisi, R., Protti, M., & Schwartz, S. (2018). Do slow slip events trigger large and great megathrust earthquakes? *Science advances*, 4(10), eaat8472.
- W. Goebel, T., Schorlemmer, D., Becker, T., Dresen, G., & Sammis, C. (2013). Acoustic emissions document stress changes over many seismic cycles in stick-slip experiments. *Geophysical Research Letters*, 40(10), 2049–2054.
- Yamada, T., Mori, J. J., Ide, S., Abercrombie, R. E., Kawakata, H., Nakatani, M., ... Ogasawara, H. (2007). Stress drops and radiated seismic energies of microearthquakes in a south african gold mine. *Journal of Geophysical Research: Solid Earth*, 112(B3).
- Yoshimitsu, N., Kawakata, H., & Takahashi, N. (2014). Magnitude-7 level earthquakes: A new lower limit of self-similarity in seismic scaling relationships. *Geophysical Research Letters*, 41(13), 4495–4502.